Structure of a Tropical Cyclone Developed in a Three-Dimensional Numerical Simulation Model

YOSHIO KURIHARA AND ROBERT E. TULEYA

Geophysical Fluid Dynamics Laboratory/NOAA, Princeton University, Princeton, N. J. 08540

(Manuscript received 29 September 1973, in revised form 23 January 1974)

ABSTRACT

A three-dimensional, 11-level, primitive equation model has been constructed for a simulation study of tropical cyclones. The model has four levels in the boundary layer and its 70×70 variable grid mesh encloses a 4000-km square domain with a 20-km resolution near the center. Details of the model, including the parameterization scheme for the subgrid-scale diffusion and convection processes, are described.

A weak vortex in the conditionally unstable tropical atmosphere is given as the initial state for a numerical integration from which a tropical cyclone develops in the model. During the integration period of one week, the sea surface temperature is fixed at 302K.

The central surface pressure drops to about 940 mb, while a warm moist core is established. The azimuthal component of mean horizontal wind is maximum at about 60 km from the center at all levels. A strong inflow is observed in the boundary layer. At upper levels, a secondary radial-vertical circulation develops in and around the region of negative mean absolute vorticity. In the same region, the azimuthal perturbation of horizontal wind is pronounced. At the mature stage, the domain within 500 km radius is supplied with kinetic energy for asymmetric flow by both barotropic and baroclinic processes. At 60 km radius, the temperature perturbation field is maintained by condensation-convection heating at upper levels and by adiabatic temperature change due to vertical motion at lower levels. An area having an eye-like feature is found off the pressure center.

Structure of spiral bands in the outer region is extensively analyzed. The phase relationship among the pressure, horizontal motion, vertical motion, temperature and moisture fields is discussed. The spiral band behaves like an internal gravity wave. Once the band is formed in an area surrounding the center, it propagates outward apparently without appreciable further supply of energy, as far as the present case is concerned.

1. Introduction

A three-dimensional numerical model has been constructed at the Geophysical Fluid Dynamics Laboratory/NOAA for the simulation study of a tropical cyclone.

The purpose of the present paper is to describe the numerical model in detail and to present a result of an experiment with emphasis on spiral bands which developed in the model.

As reviewed by Ooyama (1969), the numerical modeling study of a tropical cyclone was given a new turn by the introduction of models with implicit convection. In these models the collective effect of cumulus convection is incorporated through a parameterization method. This approach replaced the classical method in which the energy generation was directly related to a circulation in the model.

Ooyama (1969) considered the penetrative nature of clouds in the formulation of a parameterization scheme. In his model, the cloud mass flux is determined from an energy consideration and mass convergence in the boundary layer. Further sophistication of parameterization schemes of this kind has been studied (e.g., Ooyama, 1971; Arakawa, 1971).

A similar type of parameterization, in which the upward flux of energy at the top of the boundary layer is vertically distributed in one way or another based on a certain hypothesis of penetrative convection, has been used in axisymmetric tropical cyclone models (e.g., Yamasaki, 1968; Rosenthal, 1969; Sundqvist, 1970), and also in asymmetric models (e.g., Anthes et al., 1971; Mathur, 1972). The treatment of convection in these models after a moist neutral state is reached is diversified.

The so-called moist convective adjustment (Manabe et al., 1965) is presumably another kind of substitute for the convective processes. The criterion for convective adjustment is determined from local thermodynamical conditions. Such a scheme is adopted in a general circulation model and an analysis of the numerical results from the model shows that the disturbances having a warm moist core developed in the model tropics (Manabe et al., 1970).

Encouraged by the above result and also in order to avoid a change of scheme which may otherwise be required after the conditional instability is eliminated, we attempt in this study to use the convective adjustment method in a modified form. Besides the param-

eterization of the moist convection, the treatment of the horizontal and vertical diffusion processes has to be specified. Another problem in the construction of a three-dimensional model is a design of the grid system. The detail of the model structure is described in Sections 2 and 3.

Some results from a numerical simulation experiment are presented in Section 5. It is shown that the present model is capable of dealing with the growth of a weak vortex into a hurricane-like vortex and its maintenance. However, various simplifying conditions are imposed on the present model: for example, the effect of radiation is not included; constant f-plane is assumed; the integration domain is isolated in a large closed domain; and the sea surface temperature is fixed. Consequently, problems like genesis or movement of hurricanes cannot be treated. The initial flow field is under the strong constraint of the closed domain, too. Therefore, the evolution of a vortex with high similitude to an actual case (e.g., Yanai, 1968) cannot be expected from the present experiment. The present model may be considered to be a prototype of future models to be used for an expanded experimental design.

One of the merits of numerical experimentation is that a fine network of simultaneous observations is established in the model. Such observations are essential for the analysis of a moving mesoscale system such as a spiral band in a hurricane. This is shown in Section 6 and speculation on the behavior of the band is made based on such ideal observations.

2. Numerical model

a. Governing equations

A primitive equation model with a constant f-plane approximation is used in the present study. The Coriolis parameter f is fixed at 5×10^{-5} sec^{-1} which is the value at approximately 20N.

The governing equations in the σ-coordinate system originally proposed by Phillips (1957) are written as follows:

Equation of motion

$$\frac{\partial}{\partial t}(p_*u) = -\mathfrak{D}(u)+fp_*v-p_*\frac{\partial\phi_p}{\partial x}+_{H}F_x+_{H}F_x, \quad (2.1)$$

$$\frac{\partial}{\partial t}(p_*v) = -\mathfrak{D}(v)-fp_*u-p_*\frac{\partial\phi_p}{\partial y}+_{H}F_y+_{V}F_y, \quad (2.2)$$

where t is the time; u and v the x and y components, respectively, of the horizontal wind $\mathbf{V}$; and p_* the surface pressure. The operator $\mathfrak{D}$ denotes the three-dimensional-divergence

$$\mathfrak{D}(\ ) = \frac{\partial(\ )p_*u}{\partial x}+\frac{\partial(\ )p_*v}{\partial y}+\frac{\partial(\ )p_*\dot\sigma}{\partial\sigma}, \quad (2.3)$$

where $\sigma=p/p_*$, p is the pressure, and $\dot\sigma$ the vertical σ-velocity, i.e., $d\sigma/dt$. The pressure gradient force is estimated from the slope of the geopotential of an isobaric surface, ϕ_p. The last two terms in (2.1) and (2.2) represent the frictional forces due to the horizontal and vertical diffusion of the momentum, respectively.

Tendency equation

$$\frac{\partial}{\partial t}p_* = -\mathfrak{D}(1) = -\int_0^1\left(\frac{\partial p_*u}{\partial x}+\frac{\partial p_*v}{\partial y}\right)d\sigma, \quad (2.4)$$

where the boundary conditions, i.e., $\dot\sigma=0$ at $\sigma=0$ and 1, are implied.

Vertical σ-velocity

$$\sigma = \frac{1}{p_*}\left[-\sigma\frac{\partial p_*}{\partial t}-\int_0^\sigma\left(\frac{\partial p_*u}{\partial x}+\frac{\partial p_*v}{\partial y}\right)d\sigma\right] \quad (2.5)$$

Vertical p-velocity

$$\omega = \frac{dp}{dt} = -p_*\sigma\left[-\frac{\dot\sigma}{\sigma}+\frac{\partial\dot\sigma}{\partial\sigma}+\left(\frac{\partial u}{\partial x}+\frac{\partial v}{\partial y}\right)\right] \quad (2.6)$$

Hydrostatic relation

$$\frac{\partial\phi}{\partial\ln\sigma} = -R_aT, \quad (2.7)$$

or

$$\phi-R_aT = \frac{\partial\phi\sigma}{\partial\sigma}, \quad (2.8)$$

where ϕ is the geopotential of a constant σ-surface, T the temperature, and R_y the gas constant.

Thermodynamic equation

$$\frac{\partial}{\partial t}(p_*T) = -\mathfrak{D}(T)+\frac{R_a}{c_p}\frac{T\omega}{\sigma}+_{H}F_T+_{V}F_T+\text{QCON}, \quad (2.9)$$

where c_p is the specific heat of the air at the constant pressure. The last three terms represent the effects of horizontal diffusion, of vertical diffusion, and of the condensation and convection process, respectively. The effect of radiation is ignored in the present experiment.

Equation for mixing ratio of water vapor

$$\frac{\partial}{\partial t}(p_*r) = -\mathfrak{D}(r)+_{H}F_r+_{V}F_r+\text{RCON}, \quad (2.10)$$

where r is the mixing ratio of the water vapor and the meaning of the last three terms is similar to that of the corresponding terms in (2.9).

b. Grid system

The model atmosphere is divided into 11 layers. Each layer has an integer k level in it and bounded by half-integer levels. Table 1 shows the position of the levels. These positions are determined based on the consideration of energy consistency in the finite-difference scheme (Kurihara, 1968; see Section 5). The top layer in the model will establish a stable state above the troposphere. The planetary boundary layer is to be resolved by the bottom four layers.

Fig. 1 shows that the variables u, v, T, r, ω are defined at integer levels whereas ϕ and $\dot{\sigma}$ are defined at half-integer levels. The geopotential of an isobaric surface, ϕ_p, is obtained from the height of the nearest sigma surface by applying Eq. (2.7).

In the present experiment, the model atmosphere is enclosed in a 4000-km square domain by a free-slip, insulated lateral boundary. As suggested by Rosenthal (1971), a domain of at least this size is required to make the influence of a closed boundary on a system sufficiently small. The whole domain is covered by 70 times 70 boxes, each being bounded by two pairs of lines parallel to the x and y axes. The grid is placed at the center of each box and all variables are defined there. The side length of the boxes and the position of the grids are listed in Table 2 and the configuration of boxes in a part of the first quadrant is shown in Fig. 2. The central part of a domain, i.e., a 400-km square area, is resolved into uniform 20-km square boxes. Outside this area, the resolution becomes coarser as the boundary is approached. The shape of the box in the outer area is square along the diagonals of the domain and rectangular elsewhere. Note that the present variable grid system has continuous rather than
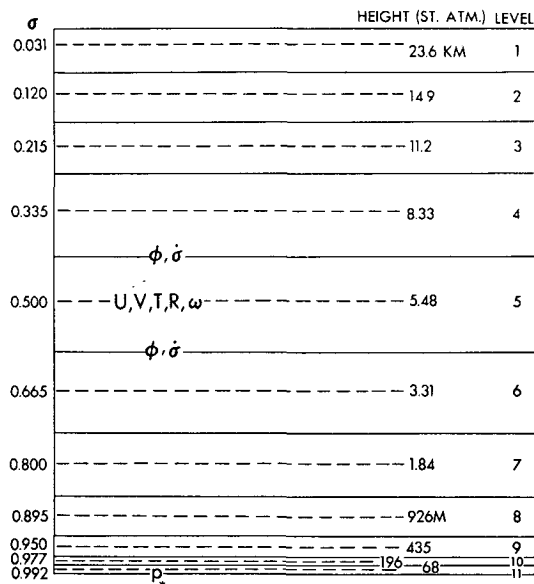

FIG. 1. Vertical division of the model atmosphere into 11 layers.

abrupt changes of grid size. Accordingly, some of the difficulties involved in a so-called nested grid are avoided.

c. Lateral boundary conditions

At the lateral boundary of the domain, there exists neither grid-scale nor subgrid-scale normal flux of any quantity. The normal component of the pressure gradient force is obtained from the geostrophic balance relation with the wind tangent to the wall.

d. Finite-difference scheme

The governing equations are time-integrated by the Euler-backward method (Matsuno, 1966; Kurihara,

TABLE 1. The σ-levels and their approximate heights.

Level k	σ	Height (m)
0.5	0.00000000	
1.0	0.03060333	23637
1.5	0.08318847	17270
2.0	0.12000000	14940
2.5	0.17310091	12616
3.0	0.21500000	11242
3.5	0.26704077	9847
4.0	0.33500000	8328
4.5	0.42025419	6738
5.0	0.50000000	5478
5.5	0.59487807	4168
6.0	0.66500000	3311
6.5	0.74338763	2424
7.0	0.80000000	1843
7.5	0.86092366	1258
8.0	0.89500000	926
8.5	0.93042512	575
9.0	0.95000000	435
9.5	0.96998671	260
10.0	0.97700000	196
10.5	0.98406400	132
11.0	0.99200000	68
11.5	1.00000000	0

TABLE 2. Grid positions and side lengths of the boxes. The x coordinate of the grid and the length Δx of the boxes along the x axis, starting from the domain center, are listed.

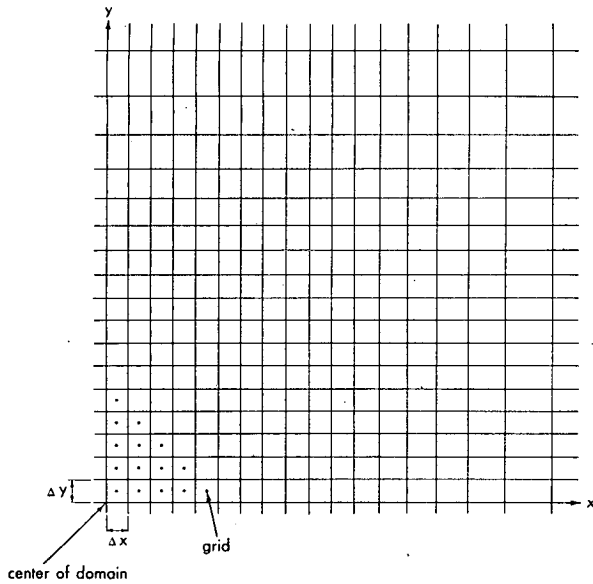| Grid or box index	x (km)	Δx (km)	Grid or box index	x (km)	Δx (km)
1	10	20	19	470.5	55
2	30	20	20	530	64
3	50	20	21	598.5	73
4	70	20	22	676	82
5	90	20	23	762	90
6	110	20	24	854.5	95
7	130	20	25	951	98
8	150	20	26	1050	100
9	170	20	27	1150	100
10	190	20	28	1250	100
11	210.5	21	29	1350	100
12	232	22	30	1450	100
13	255	24	31	1550	100
14	280	26	32	1650	100
15	307.5	29	33	1750	100
16	339	34	34	1850	100
17	376	40	35	1950	100
18	419.5	47			

FIG. 2. Horizontal grid system. A part of the first quadrant of the domain is shown.

1965). This marching process is used to suppress high-frequency gravity waves in the model.

The tendencies of wind, temperature, water vapor mixing ratio, and surface pressure are obtained from the estimates of the contributing components, i.e., the terms on the right-hand side of the governing equations. The computation scheme used is based on the box method, version II (Kurihara and Holloway, 1967), with the change of formulas for the hydrostatic relation (Kurihara, 1968, Section 2) and for the pressure gradient force and the vertical p-velocity [Holloway and Manabe (1971, Appendix A); also see p. 339 for the treatment of the truncation error in the moisture equation]. In estimating the vertical flux of moisture across the half-integer level, the average of arithmetic and geometric means of the mixing ratio at the adjacent integer levels is taken rather than a simple arithmetic mean. This is done because the decrease of mixing ratio with height is usually more rapid than linear.

In each iteration of the Euler-backward scheme, the new data for every grid point are calculated initially without including the last term of (2.9) and (2.10) which is related to the condensation process. Then, this effect is incorporated in the above obtained temperature and mixing ratio through a moist convective adjustment of the fields which will be described later.

3. Parameterization of subgrid-scale processes

a. Subgrid-scale horizontal diffusion

The subgrid-scale horizontal diffusion is treated by the nonlinear viscosity scheme given by Smagorinsky (1963). The general form of the formulation for the

σ-coordinate system (Kurihara and Holloway, 1967, Appendix 1) is simplified in writing the formulas below (for explanation, see Holloway and Manabe, 1971, p. 340).

The frictional force due to the lateral stresses are

$$_HF_x = \frac{\partial \tau^{xx}}{\partial x} + \frac{\partial \tau^{xy}}{\partial y}, \tag{3.1}$$

$$_HF_y = \frac{\partial \tau^{yx}}{\partial x} + \frac{\partial \tau^{yy}}{\partial y}, \tag{3.2}$$

where τ is equivalent to the stress tensors for the momentum mixing along constant σ surfaces and is related to the tension D_T and shearing rate of strain D_S by

$$\tau^{xx} = -\tau^{yy} = p_* \Gamma D_T, \tag{3.3}$$

$$\tau^{xy} = \tau^{yx} = p_* \Gamma D_S. \tag{3.4}$$

The definition of D_T and D_S is

$$D_T = \frac{\partial u}{\partial x} - \frac{\partial v}{\partial y}, \tag{3.5}$$

$$D_S = \frac{\partial v}{\partial x} + \frac{\partial u}{\partial y}, \tag{3.6}$$

and Γ is given by

$$\Gamma = l^2 |D|, \tag{3.7}$$

where $|D| = (D_T{}^2 + D_S{}^2)^{\frac{1}{2}}$. In the case of two-dimensional non-divergent flow, for which (3.3) is derived, D_T becomes $2(\partial u/\partial x)$ or $-2(\partial v/\partial y)$. The characteristic length l in (3.7) is obtained from

$$l = k_0 \delta, \tag{3.8}$$

where δ is the grid distance in the appropriate direction. In this study, the parameter k_0 is 0.2 for the area from the center of domain to 1800 km radius. The square of k_0 is increased from 0.04 to 0.4 linearly to a radius of 2000 km and fixed at 0.4 beyond 2000 km. Such an increase in the diffusion coefficient is made as a precaution against the development of noise near the boundary (Benwell and Bushby, 1970).[1]

The tendency of temperature and mixing ratio due to the horizontal diffusion is computed from

$$_HF_\alpha = \frac{\partial}{\partial x}\left[p_* \Gamma \left(\frac{\partial \alpha}{\partial x}\right)_p \right] + \frac{\partial}{\partial y}\left[p_* \Gamma \left(\frac{\partial \alpha}{\partial y}\right)_p \right], \tag{3.9}$$

where α stands for T or r, and the subscript p means that the gradient is taken along constant pressure surfaces.

---

[1] In the present experiment, noise was not excited near the boundary. It is not known whether the assumption of high viscosity near the boundary was needed or not.

b. Subgrid-scale vertical diffusion

The estimate of vertical diffusion process is first made for air-sea interaction. Then, the effects of free convection and of mechanical turbulence above the surface layer are evaluated, in this order.

1) AIR–SEA INTERACTION

In the Monin-Obukhov framework, the downward flux of momentum τ, sensible heat H, and water vapor E at the surface are evaluated from the formulas

$$\tau = \rho V_*^2 \frac{V(h)}{|V(h)|},\qquad (3.10)$$

$$H = \rho c_p |V_*| \theta_*,\qquad (3.11)$$

$$E = \rho |V_*| r_*,\qquad (3.12)$$

where ρ is the density of air, V_* the friction velocity, θ_* the frictional potential temperature, and r_* the friction mixing ratio. The lowest integer level of the model, which is ~ 68 m above sea level, is assigned to the height h to be chosen within the constant flux layer.

The quantities V_*, θ_* and r_* are obtained, when $V(h)$, $\theta(h)$ and $r(h)$ are given and the surface values $\theta(0)$ and $r(0)$ are specified, by solving the following simultaneous relations by an iterative method:

$$|V(h)| = |V_*| \left[f_m\left(\frac{h}{L}\right) - f_m\left(\frac{z_0}{L}\right) \right],\quad (3.13)$$

$$\theta(h) - \theta(z_0) = \theta_* \left[f_h\left(\frac{h}{L}\right) - f_h\left(\frac{z_0}{L}\right) \right],\quad (3.14)$$

$$r(h) - r(z_0) = r_* \left[f_r\left(\frac{h}{L}\right) - f_r\left(\frac{z_0}{L}\right) \right].\quad (3.15)$$

In the above relations, L is the Monin-Obukhov length

$$L = -\frac{\rho c_p T |V_*|^3}{kgH} = \frac{T |V_*|^2}{kg\theta_*},\qquad (3.16)$$

where k is von Kármán's constant and g the acceleration of gravity, and Charnock's relation is used to give the roughness length z_0 (see Delsol et al., 1971, p. 187)

$$z_0 = 0.032 \frac{|V_*|^2}{g}.\qquad (3.17)$$

In addition, $\theta(z_0)$ in (3.14) and $r(z_0)$ in (3.15) must be related to $\theta(0)$ and $r(0)$. In the present model, the relationship which was tentatively used by Sasamori (1970, p. 1126) and allows for the jump of T and r at the interfacial layer is adopted;

$$K_{sh} \frac{\theta(z_0) - \theta(0)}{z_0} = |V_*| \theta_*,\qquad (3.18)$$

$$K_{sr} \frac{r(z_0) - r(0)}{z_0} = |V_*| r_*,\qquad (3.19)$$

where $K_{s\alpha} = |V_*| z_0 / [2\varphi_\alpha(z_0/L)]$, α standing for h and r. The functions f_m, f_h and f_r in (3.13)–(3.15) are defined as $f_m = \int \varphi_m d[\ln(z/L)]$, etc., where φ_m, φ_h and φ_r are semi-empirically determined functions. The functions φ used in this study are the same with those adopted in the numerical experiments by Delsol et al. (1971, p. 186). The sea surface temperature of the model is fixed at 302K and $r(0)$ is the saturation mixing ratio at the sea-surface.

2) FREE DRY CONVECTION

In the present model, the effect of free convection is incorporated before that of mechanical turbulence is computed. At first, the heat and moisture transported across the surface is temporarily stored in the lowest layer. If this establishes an absolutely unstable condition between the levels 11 and 10, the dry convective adjustment which will be described below is applied to neutralize it. A similar check and adjustment between two levels proceeds upward and is iterated until a gravitationally unstable state is eliminated. Such a scheme is presumed to be a substitute for the process of free convection with which condensation is not accompanied.

In the dry convective adjustment, the virtual temperature T_v is corrected whenever the stratification is absolutely unstable, i.e., when $-\partial T_v/\partial z > g/c_p$, under conditions involving conservation of the total potential energy and moisture content. The use of T_v means that the density considered here is that of the moist air. In practice, it is very convenient to linearize T_v; i.e., $T_v = T + 0.61\bar{T}r$, where $\bar{T}$ is the mass-weighted average temperature for the two levels and is invariant for the exchange of heat between the levels. There is no unique method to determine the corrections of T and r from that of T_v. In the present study, the corrections for T and r are obtained by multiplying the correction for T_v by the lower level values of T/T_v and r/T_v, respectively.

3) MECHANICAL TURBULENCE

Vertical mixing above the surface layer due to mechanical turbulence is parameterized by making use of the eddy diffusion coefficient technique, where the diffusive fluxes of momentum, heat and moisture are written, respectively, as

$$\tau = \rho K_M \frac{\partial V}{\partial z},\qquad (3.20)$$

$$H = \rho c_p K_H \frac{\partial \theta}{\partial z},\qquad (3.21)$$

$$E = \rho K_H \frac{\partial r}{\partial z}. \tag{3.22}$$

The value of the coefficient is different for the transport of momentum and that for heat. The coefficient for moisture is assumed to be equal to that for heat.

In the present model, the Richardson-number-dependent diffusion coefficient is obtained based on the extensive application of Ellison's heuristic theory, although it was developed originally for the surface layer.

According to Ellison (1957), the ratio K_H/K_M is expressed as

$$\frac{K_H}{K_M} = b\left(1 - \frac{\text{Rf}}{c}\right)(1 - \text{Rf})^{-2}, \tag{3.23}$$

where Rf is the flux Richardson number, c its critical value (Rf $\leqslant c$), and b the value of K_H/K_M at the neutral condition (Ri = Rf = 0). In this study, c and b are specified as 0.1 and 1, respectively. Since K_H/K_M = Rf/Ri, where Ri is the Richardson number, (3.23) yields the equation which determines Rf for given Ri:

$$(\text{Rf})^3 - 2(\text{Rf})^2 + \left(1 + \frac{b}{c}\text{Ri}\right)(\text{Rf}) - b\,\text{Ri} = 0. \tag{3.24}$$

With the use of c and b specified above, one positive real root is obtained from (3.24) for a given Ri which is non-negative because the free dry convection has eliminated any unstable state. The Richardson number for the moist air may be defined as

$$\text{Ri} = \frac{g}{T}\left(\frac{\partial T}{\partial z} + \frac{g}{c_p} + 0.61T\frac{\partial r}{\partial z}\right)\left(\frac{\partial V}{\partial z}\right)^{-2}. \tag{3.25}$$

It is suggested by Ellison (1957) that K_M may be proportional to $[1 - (\text{Rf}/c)]^{\frac{1}{2}}$. In the present model, K_M is determined from

$$K_M = l^2 \left|\frac{\partial V}{\partial z}\right|\left(1 - \frac{\text{Rf}}{c}\right)^{\frac{1}{2}}, \tag{3.26}$$

where l is the mixing length for the neutral condition and is set equal to 30 m; K_H is obtained from

$$K_H = K_M \frac{\text{Rf}}{\text{Ri}}. \tag{3.27}$$

Diffusion coefficients, particularly K_H, become fairly small for a large value of Ri.

The tendencies of $p_* V$, $p_* T$ and $p_* r$ due to the mechanical turbulence are $-g\partial\tau/\partial\sigma$, $-g\partial H/\partial\sigma$ and $-g\partial E/\partial\sigma$, respectively. For computational stability, the changes due to these effects are evaluated by an implicit scheme (Richtmyer, 1957, pp. 101–104). It should be noted that the flux of heat and moisture at the surface has already been taken into account by the scheme for free dry convection.

In summary, the total effect of the vertical diffusion process may be written as:

$$vF_{(x,y)} = -g\frac{\partial\tau}{\partial\sigma} \tag{3.28}$$

$$vF_T = -g\frac{\partial H}{\partial\sigma} + (\text{effect of free dry convection}) \tag{3.29}$$

$$vF_r = -g\frac{\partial E}{\partial\sigma} + (\text{effect of free dry convection}) \tag{3.30}$$

c. Moist convective adjustment

The details of the moist convective adjustment which is applied to the present model, including the computational procedures, are described by Kurihara (1973). An outline of the scheme follows.

1) CONDITION FOR FREE MOIST CONVECTION

It is assumed that free moist convection may start to develop when the height change of temperature of a rising cloud element is greater than the lapse rate of a cloud environment. That is, the condition to be satisfied at the cloud base, which can be at any height, is

$$\left(\frac{dT}{dz}\right)_c > \left(\frac{\partial T}{\partial z}\right)_e, \tag{3.31}$$

where the subscripts c and e are used to indicate a quantity for the cloud element and for the environment, respectively. It is possible that a cloud element may become buoyant even when T_c is slightly lower than T_e at or near the cloud base because of the density correction for moisture. However, for simplicity, the conditions $T_c = T_e$ at the cloud base and $T_c > T_e$ at a height slightly above the cloud base are presupposed in deriving (3.31).

For a hypothetical cloud element with an entrainment rate E, (3.31) takes the form

$$-\gamma_m - \frac{L}{c_p + (L\epsilon/p)(de_s/dT)}[(r_s)_e - r_e]E > \left(\frac{\partial T}{\partial z}\right)_e, \tag{3.32}$$

where γ_m is the moist adiabatic lapse rate, L the latent heat of condensation, $\epsilon = 0.622$, e_s the saturation vapor pressure, and r_s the saturation mixing ratio.[2] Note that the term expressing the entrainment effect in (3.32) involves a factor $(r_s)_e - r_e$, instead of $r_c - r_e$, so that the mixing effect of temperature as well as water vapor is implicitly included. It is seen from (3.32) that conditions are more favorable for moist convection if

---

[2] Use has also been made of the fact that $de_s/dT = L\epsilon e_s/(RT^2)$ from the Clausius-Clapeyron equation.

(i) the stratification is conditionally more unstable, (ii) the relative humidity is higher, and (iii) an entrainment into a cloud element is less. Practically, T and r which appear in the governing equations can be taken for T_e and r_e.

The fractional entrainment rate for a cloud element is given by the relation used in a plume or a bubble model of cloud, i.e.,

$$E = 0.2D^{-1}, \qquad (3.33)$$

where D is the radius of the element. In the actual atmosphere, each cloud element has different size. Little is known, however, about the factors which determine the size of elements. In the present scheme, for simplicity, only one cloud size is evaluated for a given moisture field. In other words, D is determined from the relation

$$D = D_0 (r/r_s)^{\frac{1}{2}}, \qquad (3.34)$$

which makes moist convection impossible when $r = 0$; D_0 is specified as 500 m.

2) ADJUSTMENT OF TEMPERATURE AND MIXING RATIO

The effects of the ensemble cumulus convection on the horizontally averaged temperature and mixing ratio are represented as apparent heat and moisture sources. The following two equations approximately express these effects for the case of a pseudo-adiabatic process. Although the equations in this form are not used explicitly in the present model, they are written so the present parameterization scheme may be compared to them. The equations are

$$\frac{\partial T}{\partial t} + \cdots = \frac{L}{c_p} C - \frac{\partial}{\rho \partial z}[M_c(T_c - T_e)], \qquad (3.35)$$

$$\frac{\partial r}{\partial t} + \cdots = -C - \frac{\partial}{\rho \partial z}[M_c(r_c - r_e)], \qquad (3.36)$$

where C is the rate of condensation per unit mass of dry air and M_c denotes the total mass flux in the cloud. The transport in the cloud, $M_c T_c$ and $M_c r_c$, and that in the environment by the compensating downward flux, $-M_c T_e$ and $-M_c r_e$, are combined to yield the last term in the above equations, i.e., the upward fluxes of the excess temperature, $T_c - T_e$, and the excess mixing ratio, $r_c - r_e$, in the cloud.

In the present scheme, the above-mentioned fluxes of excess temperature and excess mixing ratio during a marching step Δt, which will be denoted by F_T and F_r, are not evaluated explicitly from the cloud mass flux, but rather treated kinematically based on some speculations on the moist convection. Yet, by analogy with (3.35) and (3.36), the terms QCON and RCON in (2.9) and (2.10) may take the forms

$$(\text{QCON}/p_*)\Delta t = q + \frac{\partial}{\partial \sigma}F_T, \qquad (3.37)$$

$$(\text{RCON}/p_*)\Delta t = -w + \frac{\partial}{\partial \sigma}F_r, \qquad (3.38)$$

where w is the amount of condensation per unit mass of dry air per period Δt, and q is the temperature increase due to the released heat.

The overall effect of the cumulus convection is to stabilize a large-scale thermodynamical state. This is achieved by the decrease of latent energy in the lower layers and the upward transport of released latent heat in the form of the flux of the excess temperature. It is presumed in the present scheme that this kind of process takes place even locally. In other words, when a state between the two neighboring levels is favorable for free moist convection, condensation occurs at the lower level and heat and water vapor are transported from the lower to the upper level so that a local neutralization would be achieved if those processes could be isolated. Thus, a pre-existing unstable state is destroyed, although the resulting heat flux may establish a new unstable state for the next iteration. It is expected that the integral of such local processes over whole iterations brings about the overall stabilization and the convection ceases eventually. The adjustment of the fields is complete at this point. The equations for q, w, F_T and F_r are derived from this hypothesis.

Assume that a state of T and r at a layer k is favorable, when compared with the conditions of layer $k-1$, for the occurrence of free moist convection. Then, as a result of condensation in the layer k and the upward fluxes F_T and F_r across the level $k-\frac{1}{2}$, T and r at the level k and $k-1$ are changed to T_* and r_*; i.e.,

$$\left.\begin{aligned}
T_k^* &= T_k + q_k - [(F_T)_{k-\frac{1}{2}}/m_k] \\
r_k^* &= r_k - w_k - [(F_r)_{k-\frac{1}{2}}/m_k] \\
T_{k-1}^* &= T_{k-1} + [(F_T)_{k-\frac{1}{2}}/m_{k-1}] \\
r_{k-1}^* &= r_{k-1} + [(F_r)_{k-\frac{1}{2}}/m_{k-1}]
\end{aligned}\right\}, \qquad (3.39)$$

where m is air mass per unit area in a layer. The energy relation between q_k and w_k is

$$w_k = \frac{c_p}{L}q_k. \qquad (3.40)$$

According to this hypothesis, T^* and r^* should represent a state which is just critical to a free moist convection. The formula corresponding to (3.32) under such a state is

$$-\gamma_m^* - \frac{L}{c_p + (L\epsilon/p)(de_s/dT)^*}(\overline{r_s^* - r^*})E_k^*$$

$$= \frac{T_{k-1}^* - T_k^*}{(z_{k-1} - z_k)^*}, \qquad (3.41)$$

where the asterisk indicates that T^* and/or r^* are used to estimate the asterisked terms and the overbar denotes the average for the two levels, weighted by the
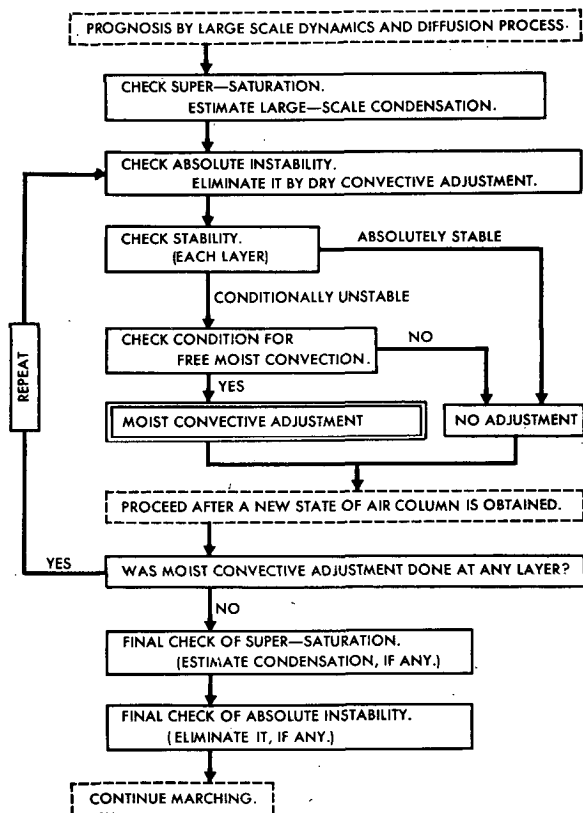
FIG. 3. Flow chart of the scheme of moist convective adjustment.

mass in each layer. By virtue of (3.39) and (3.40), Eq. (3.41) gives a relation involving q_k, $(F_T)_{k-\frac{1}{2}}$ and $(F_r)_{k-\frac{1}{2}}$.

An assumption is made here which relates the flux $(F_T)_{k-\frac{1}{2}}$ to the total released latent heat in the layer k in the simple kinematical form

$$(F_T)_{k-\frac{1}{2}} = \lambda q_k \delta_k \sigma, \qquad (3.42)$$

where $\delta_k \sigma = \sigma_{k+\frac{1}{2}} - \sigma_{k-\frac{1}{2}}$. The proportionality coefficient λ represents the efficiency of the convective transport, and the partition ratio of the released heat into the two layers, $k-1$ and k, is indicated by $\lambda/(1-\lambda)$. In the present model, λ is determined from

$$\lambda = \max\left[\frac{1}{1+(\delta_k\sigma/\delta_{k-1}\sigma)}, \ \min\left(\frac{0.15}{\delta_k\sigma}, 0.9\right)\right], \qquad (3.43)$$

where max or min (a,b) means the larger or the smaller value of the two arguments a and b (for details, see Kurihara, 1973). With λ as given above, stabilization of a state is assured.

As seen from (3.35) and (3.36), the ratio $(F_r)_{k-\frac{1}{2}}/(F_T)_{k-\frac{1}{2}}$ represents the ratio of excess mixing ratio to excess temperature in the cloud at the interface level. The change of the thermodynamical state of a rising cloud element may be nearly moist adiabatic, unless the entrainment is quite large. Accordingly, the excess

value of a quantity is supposedly large when that quantity in the environment decreases rapidly with height. Therefore, an approximate formula may be written as

$$\frac{(F_r)_{k-\frac{1}{2}}}{(F_T)_{k-\frac{1}{2}}} = \frac{r_k^* - r_{k-1}^*}{T_k^* - T_{k-1}^*}. \qquad (3.44)$$

From the above three equations [(3.41), (3.42), (3.44)], the three quantities q_k, $(F_T)_{k-\frac{1}{2}}$ and $(F_r)_{k-\frac{1}{2}}$ can be obtained. Such a procedure is applied to every set of two sequential levels and the correction of T and r is computed by (3.37) and (3.38). The above correction is iteratively made until the possibility of free moist convection is eliminated from the whole air column. Fig. 3 shows the flow chart of the iterative scheme of the adjustment. In the chart, the large-scale condensation represents the change of T and r in a single layer from a state of supersaturation to that of saturation under the condition that the sum of $c_p T$ and Lr is conserved.

4. Initial conditions and time integration

a. Initial conditions

The initial condition for the time integration is characterized by a large weak circular vortex in gradient wind balance in a conditionally unstable model atmosphere.

Specifically, the initial field is computed in the following manner:

1) A tentative azimuthal flow V, which is a function of σ and the radius R, is assumed:

$$V(R,\sigma)=\begin{cases}\dfrac{\sigma}{0.9}V(R,0.9), & \text{for} \quad \sigma<0.9 \\[2mm] V(R,0.9), & \text{for} \quad 0.9\leqslant\sigma\leqslant\sigma_{11}\end{cases} \qquad (4.1)$$

where $V(R,0.9)$ is given by

$$V(R,0.9)=\hat{V}\frac{2(R/\hat{R})}{1+(R/\hat{R})^3}. \qquad (4.2)$$

In the present experiment, we assume $\hat{V}=12$ m sec^{-1} and $\hat{R}=200$ km.

2) An approximate formula of the thermal wind is applied for (4.1) to yield

$$\frac{\partial T}{\partial R}=\begin{cases}-\dfrac{\sigma}{0.9}\dfrac{f}{R_g}V(R,0.9), & \text{for} \quad \sigma<0.9 \\[2mm] 0, & \text{for} \quad 0.9\leqslant\sigma\leqslant\sigma_{11}\end{cases} \qquad (4.3)$$

where R_g is the gas constant. Accordingly, with specification of T at a large radius, e.g., $T(5000,\sigma)$, $T(R,\sigma)$ is obtained from the integration of (4.3).
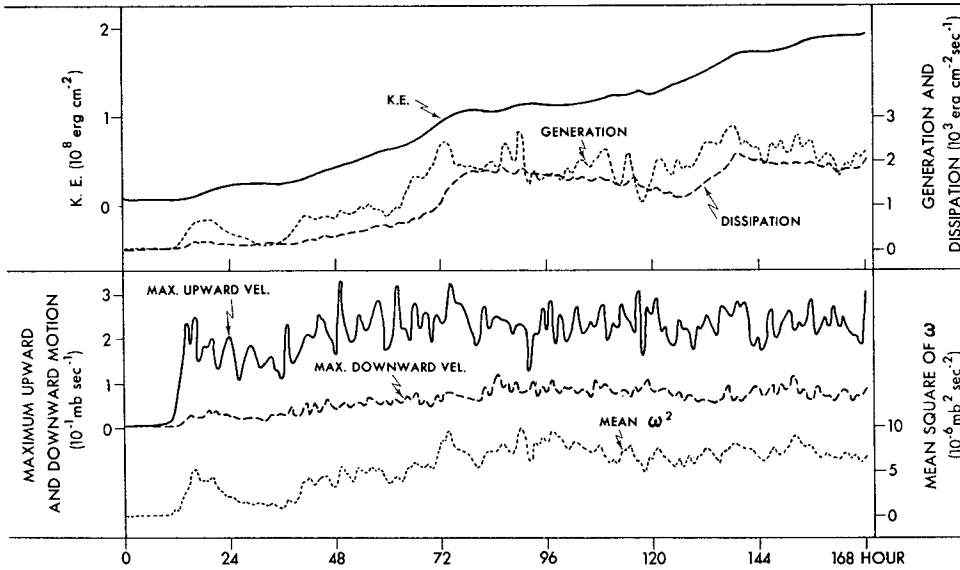
FIG. 4. Time variation of total kinetic energy, kinetic energy generation, and dissipation; also time variation of the maximum upward and downward velocity, and the mean square of ω.

3) A geostrophic wind relation near the surface gives

$$\frac{\partial p_*}{\partial R} = \rho f V(R, 0.9). \qquad (4.4)$$

From (4.4) and a specification of $p_*(5000)$, $p_*(R)$ is easily obtained. In this study, $p_*(5000) = 1010$ mb and $\rho = 1.56 \times 10^{-3}$ gm cm^{-3} are used.

4) The gradient wind V_{gr} is computed for each level at a discrete distance, which is equal to the value x listed in Table 2, by the finite-difference analogue of

$$\frac{V_{gr}^2}{R} + f V_{gr} = \frac{\partial \phi_p}{\partial R}. \qquad (4.5)$$

5) This value of V_{gr} is interpolated to all grid points and decomposed into u and v.

6) The relative humidity at each level is specified, and the mixing ratio is computed.

TABLE 3. Temperature $T(5000, \sigma)$ and relative humidity used for setting the initial conditions.

Level	σ	$T(5000,\sigma)$ (°K)	Relative humidity (%)
1	0.031	218.7	0
2	0.120	200.3	0
3	0.215	223.9	5
4	0.335	247.4	10
5	0.500	267.8	30
6	0.665	281.1	60
7	0.800	289.9	75
8	0.895	294.9	85
9	0.950	297.7	90
10	0.977	299.1	95
11	0.992	299.8	98

In Table 3, $T(5000,\sigma)$ and the specified values of relative humidity are listed. $T(5000,\sigma)$ is determined by adding 0.7K to the 10N data taken from Geophysical Memoirs No. 101 (Meteorological Office, England, 1958). Relative humidity is chosen rather arbitrarily, but not unrealistically.

The initial temperature field thus obtained is almost horizontally uniform. The difference in T between the center and the boundary is 0.9K at level 8. It is 0.03K at level 1. The surface pressure p_* decreases gradually from 1009.77 mb at $R = 1950$ km to 1005.63 mb at 10 km. The mixing ratio is about 22 gm kg^{-1} at level 11 and about 16 gm kg^{-1} at level 8.

The equivalent potential temperature is approximately 355, 327 and 350K at levels 11, 5 and 2, respectively. This indicates a conditionally unstable state.

The maximum gradient wind of the initial vortex is 8.64 m sec^{-1} at level 11 and $R = 190$ km. The wind at level 11 is greater than 5 m sec^{-1} for the range $R = 90$ to 420 km. The wind decreases roughly linearly with σ and it is less than 1 m sec^{-1} at levels 1 and 2. It is also less than 1 m sec^{-1} at all levels beyond $R = 1100$ km.

b. Time integration

Starting from the above initial state, the time integration is performed for a period of 168 hr. The time step for the Euler-backward marching scheme is 45 sec until 48 hr, when it is reduced to 30 sec. The latter value is nearly optimum to suppress an oscillation with a period of 240 sec which tends to develop in the model.

In the upper part of Fig. 4, the time variation of the area mean total kinetic energy during the integration period is shown. It keeps increasing, from 0.63 J cm^{-2} at Hour 0 to 19.3 at Hour 168, as the generation of
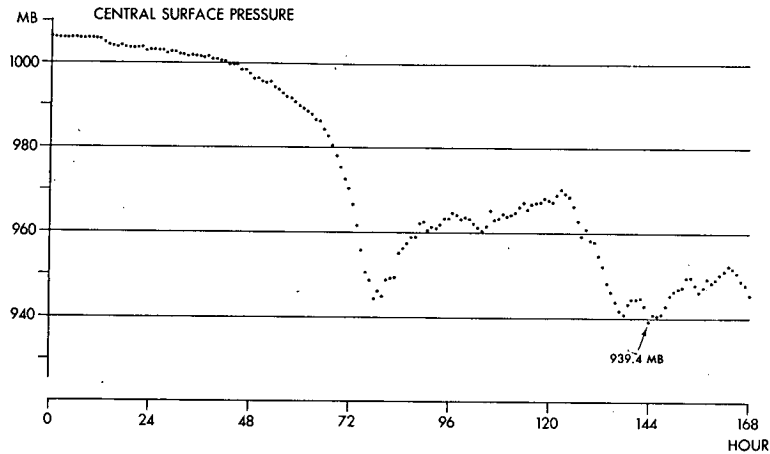
Fig. 5. Time variation of minimum surface pressure.

kinetic energy is generally larger than the dissipation as shown in the same figure. A quasi-stationary state is not reached by the domain integral of other quantities either. For example, the area mean total potential energy at Hour 168 is 2.6975×10^5 J cm^{-2}, as compared to 2.682×10^5 at Hour 0, and still indicates a positive tendency. This may be due to the lack of any radiational effects in the present model. The relative angular momentum of the whole system should keep decreasing since the surface wind is cyclonic everywhere during the integration period. It will be shown later that the moisture content for the total domain keeps decreasing during the whole period.

Although the present system as a whole has a certain trend as mentioned above, the state in the central region settles in quasi-equilibrium after a strong hurricane-like vortex evolves in the model. For example, the lower part of Fig. 4 shows that the maximum upward motion, which is usually observed in the central region, fluctuates around 0.24 mb sec^{-1} after Hour 48, while that of the downward motion fluctuates around 0.08 mb sec^{-1} after Hour 80. The maximum horizontal wind speed (not shown in figure) levels off at about 70 m sec^{-1}. After this essentially steady state is established in the central region, i.e., after Hour 80 in the present experiment, a model tropical cyclone may be said to be in its mature stage.

The average of ω^2 for all the grid points is a parameter which can be used to measure the computational behavior of a numerical model. Its time variation is also shown in Fig. 4. A stable integration is indicated by the leveling off of ω^2 at around 7×10^{-6} mb^2 sec^{-2}.

5. A simulated tropical cyclone

a. Time variation of surface elements

Fig. 5 shows the hourly values of the minimum surface pressure. It is seen that a deep tropical cyclone develops in the model in about 80 hours after the

start of time integration. The pressure drop for the one-day period ending at Hour 78 is 50 mb. In the present experiment, the central pressure increases after
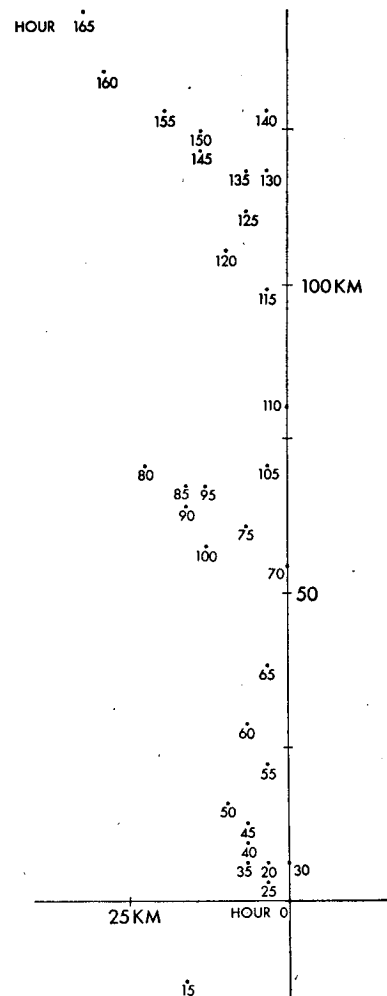

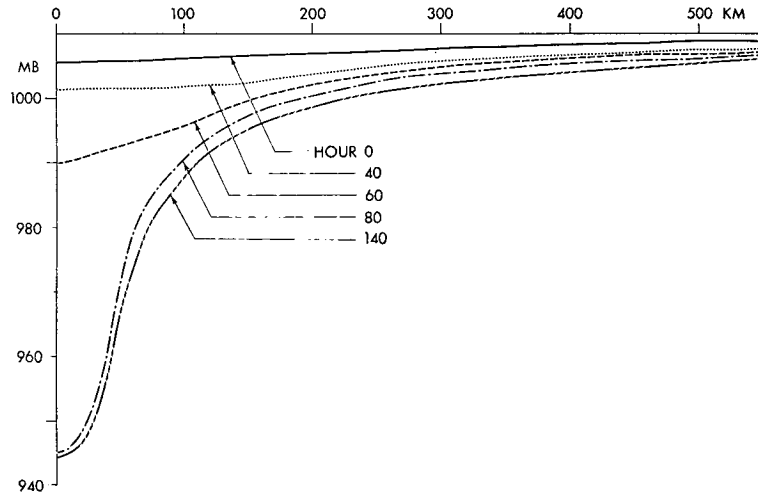Fig. 6. Location of the center of the storm.

FIG. 7. Radial distribution of $\bar{p}_*$ at Hours 0, 40, 60, 80 and 140.

the above rapid development and a secondary deepening takes place after Hour 123. The lowest value is 939.4 mb at Hour 144.

In the present analysis, the pressure center, i.e., the position of the minimum surface pressure, is used to define the center of the storm. It is located at the domain center at Hour 0. However, it later moves away from the domain center rather erratically. The center of the storm is plotted every 5 hr after Hour 15 in Fig. 6. The storm is about 100 km off the domain center in the later period, but the central region of the storm is still in the uniform fine-resolution area.

The overbar notation will be used in the present section to represent the azimuthal average of a quantity along a certain fixed radius around the storm center.

In Fig. 7, the radial distribution of $\bar{p}_*$ at different time levels is shown. It is seen that the total mass inside 500 km radius keeps decreasing even after a sharp drop of the central pressure ends at Hour 80. The field of p_* is always almost axisymmetric. The standard deviation of p_* on a circle around the center occasionally exceeds 1 mb only inside 100 km radius. Beyond 100 km, it is less than 1 mb.

The maximum wind speed at level 11 is plotted every hour in Fig. 8. Winds of fresh gale force, i.e., 17 m sec^{-1}, are observed at Hour 40 and hurricane force winds are attained at Hour 67. The maximum in the whole integration period is 56.3 m sec^{-1} at Hour 139. It is noted here that the maximum wind speed in the model is usually about 30% greater than the maximum
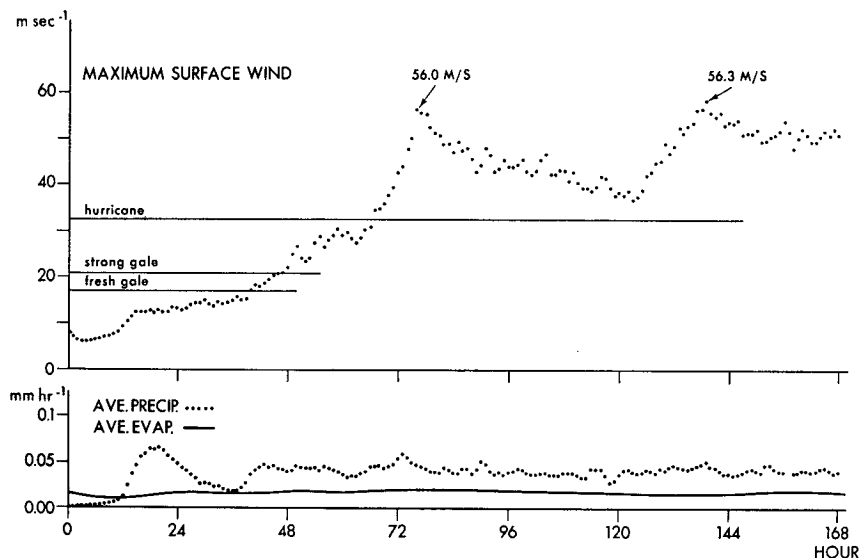

FIG. 8. Time variation of maximum wind speed at level 11, area-average precipitation,
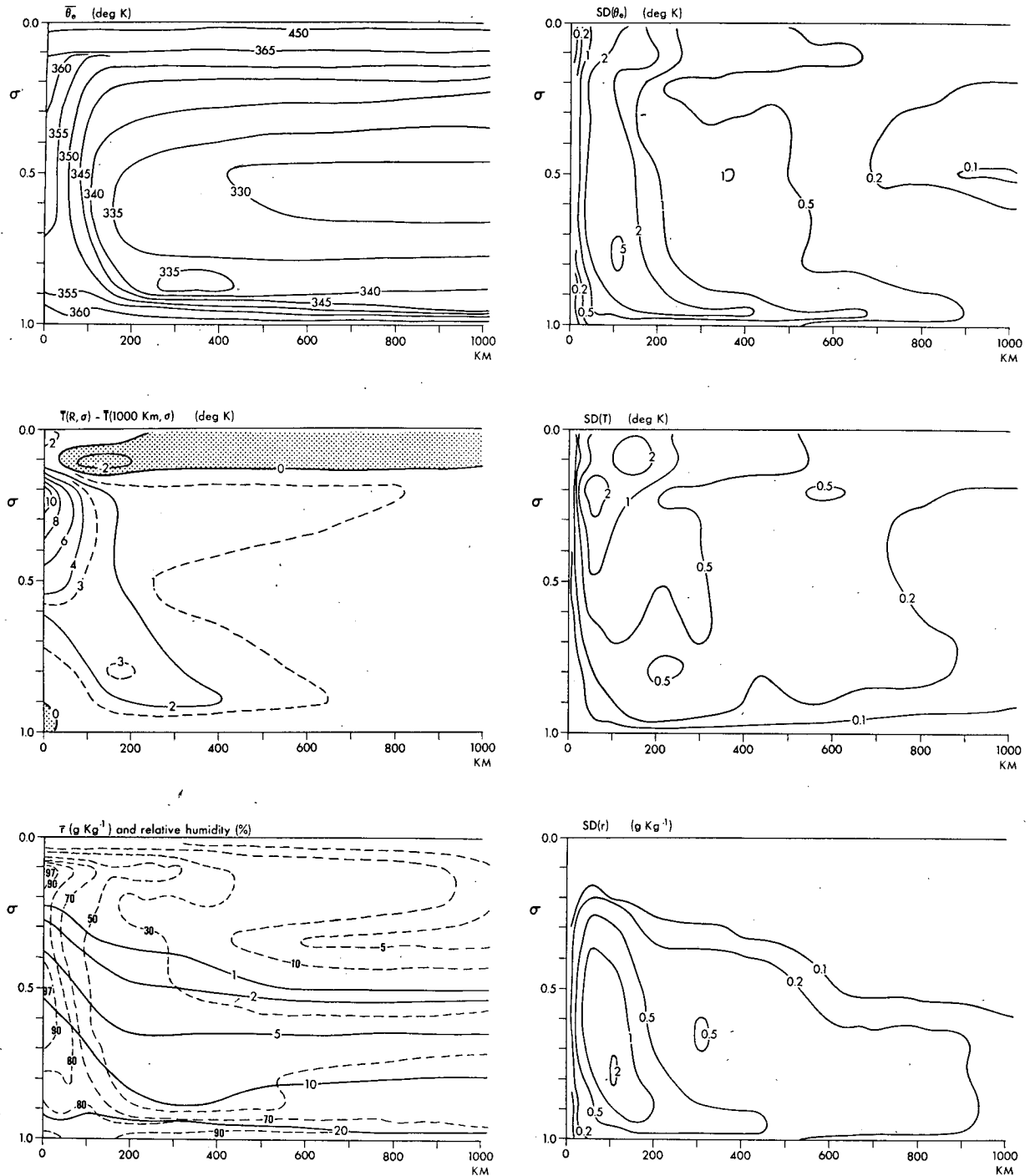and area-average evaporation.

FIG. 9. Height-radius distribution of the azimuthal mean of equivalent potential temperature (top), temperature departure from the value at 1000 km radius (middle), and mixing ratio and relative humidity (bottom), all at Hour 151. In the right half of the figure, the distributions of the standard deviation of θ_e (top), T (middle) and r (bottom) are shown.

surface wind. The extreme in the model is 77.6 m sec^{-1} obtained at Hour 138. The horizontal wind at level 11 has a component of strong inflow and is fairly symmetric as will be shown later.

The time variation of the area averages of precipita-

tion and evaporation are also shown in Fig. 8; the former is usually larger than the latter. This results in a gradual decrease in the mean precipitable water of the model, i.e., a decrease from 5.03 gm cm^{-2} in the beginning to 4.67 at the end of the integration. The

mean precipitation for the total domain is very small because the rainfall outside of the storm region is negligibly small. The maximum local intensity of the precipitation at each time step after the development of the storm is of the order of 2 mm min^{-1}.

b. Thermodynamical structure at the mature stage

In the analysis of the present experiment, Hour 151 is chosen to be a time level representative of the mature stage of the simulated tropical cyclone. At first, the thermodynamical field at the mature stage is examined.

The top left part of Fig. 9 shows the distribution of $\bar{\theta}_e$ on a radius-height plane, where θ_e is the equivalent potential temperature. The conditional instability which existed in the initial condition is almost neutralized in the central area of about 80 km radius. At Hour 20, the maximum $\bar{\theta}_e$ observed on level 5 is 336K at 150 km radius. This is about a 9K increase from Hour 0. Such an increase of $\bar{\theta}_e$ at such a large distance is related to the initial large size of the weak vortex. Then, as the vortex shrinks, the position of maximum $\bar{\theta}_e$ approaches the center; thus, the maximum (337K) at Hour 40 is at 125 km while its value (339K) at Hour 60 is at 75 km. A rapid increase of $\bar{\theta}_e$ takes place between Hours 60 and 80 in the central area. The maximum $\bar{\theta}_e$ on level 5 at Hour 80 is 357K at the center. A neutralized area expands slowly after Hour 80, and, finally, the distribution shown in the figure is obtained.

The neutralization of the conditional instability means the build-up of a warm moist core. The middle left part of Fig. 9 shows the departure of $\bar{T}$ from that at 1000 km radius, where the stratification is still conditionally unstable. The largest departure is 11K and is located slightly below level 3 at the center. At levels 1 and 2, small negative values are found, meaning relatively lower temperatures than that at 1000 km. The existence of a cold region in the upper troposphere and lower stratosphere above actual hurricanes was noted by Koteswaram (1967). At levels 7 and 8, the deviation is largest at around 150 km. At levels 10 and 11 (i.e., near the surface) $\bar{T}$ is almost constant and a very weak negative deviation is found near the center.

The moisture field, i.e., the distribution of $\bar{r}$ and the mean relative humidity, is shown in the bottom left part of Fig. 9. The air in the central region is very moist throughout the troposphere. Beyond 150 km radius, the relative humidity at levels 2 and 3 is higher than that at level 4. Note that the initial relative humidity at level 2 is zero.

In the present model, the asymmetric structure evolves in the course of integration, although the initial state is axially symmetric. The initial asymmetry is caused by the asymmetric round-off of computation. In order to express the degree of asymmetry, the standard deviation of various quantities along the circles around the storm center has been computed at different radii and different levels. This will be denoted by SD( ).

The distribution of SD(θ_e), SD(T) and SD(r) is shown in the right half of Fig. 9. The field of SD(θ_e) indicates that the thermodynamical structure is fairly axisymmetric except for the region inside 200 km and the boundary layer within 700 km from the center. In the upper central region, SD(θ_e) is 2–3K and this is largely due to SD(T). In the lower troposphere, however, SD(T) is very small and SD(r) contributes to the large SD(θ_e), the maximum of which is 5.5K at level 7 and at 100 km radius.

c. Dynamical structure at the mature stage

During the transient period when the deepening of the surface pressure and the build-up of the warm moist core take place, interrelated dynamical changes are observed in the model such as the development of strong inflow toward the center at the lower levels; the development of outflow at level 2 (i.e., below the tropopause); the intensification of cyclonic flow at all levels in the central region and at the low levels outside; and the appearance of anticyclonic flow at the upper levels outside of a few hundred kilometers from the center.

The distribution of the mean azimuthal flow, mean radial flow, and vertical motion at the mature stage is shown in the left part of Fig. 10. In the distribution of $\bar{v}_\theta$, the maximum at each level is found at about 60 km radius and hence there is no significant tilt of the line connecting the wind maximum at different levels. The radial distance of the position of maximum wind seems to be too large compared to actual hurricanes (e.g., Hawkins and Rubsam, 1968). This may be due to the inadequate grid resolution of the present model. It is also seen that $\bar{v}_\theta$ increases from the surface to level 9 at each radius and it decreases gradually with height above level 9 outside 200 km radius. Below level 4, the mean relative vorticity computed from $\bar{v}_\theta$ is greater than 10^{-4} sec^{-1} inside 140 km radius and greater than 10^{-3} sec^{-1} inside 60 km. The maximum value is 3.02 $\times 10^{-3}$ sec^{-1} at the center at level 9. The relative vorticity becomes negative at the upper levels outside about 100 km radius and at the middle levels outside 200 km. In the region bounded by the dashed lines in Fig. 10, the absolute vorticity shows very small negative values.

The distribution of $\bar{v}_r$ shows strong inflow in the boundary layer. It is different from $\bar{v}_\theta$ in that the maximum intensity of $\bar{v}_r$ is found at the lowest level. Another feature of $\bar{v}_r$ is the development of a symmetric radial-vertical circulation in the upper layers. This secondary circulation is found in and around the region of negative absolute vorticity. It is noted here that a similar structure also developed in the axisymmetric model which is analogous to the present model, when the negative absolute vorticity intensified to a certain degree. Although the negative absolute vorticity alone does not imply dynamical instability in a baroclinic circular vortex (e.g., Yanai, 1961; Ooyama,
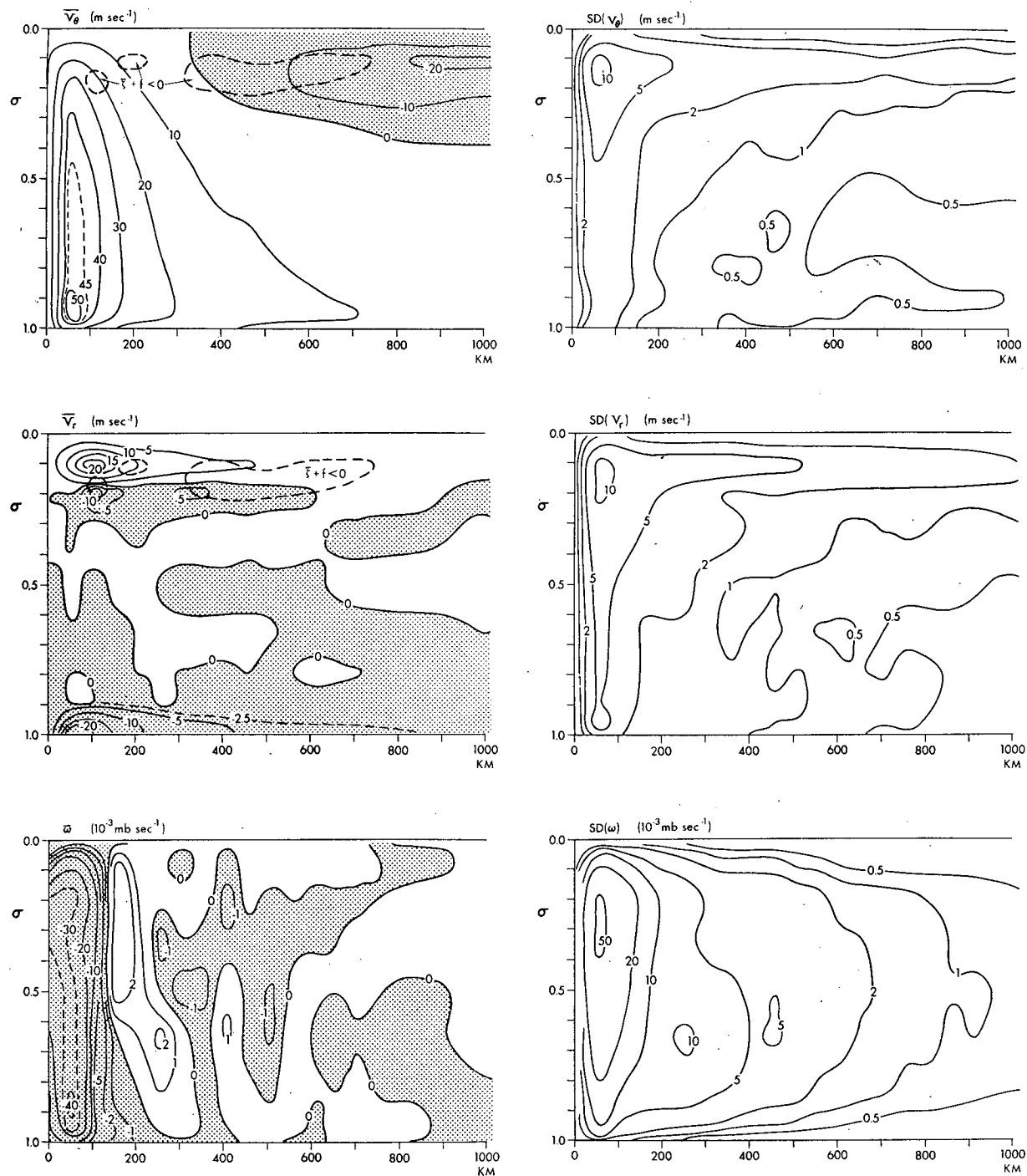
FIG. 10. Height-radius distribution of the azimuthal mean of azimuthal flow (top), radial flow (middle), and vertical p-velocity (bottom), all at Hour 151. The distribution of the standard deviation of each quantity is shown in the right half of the figure.

1966), its intensification seems to be a contributing factor for the evolution of $\bar{v}_r$ in the upper layers in the present case. The intensity of mean outflow in the present model is larger than that observed in actual hurricanes (Black and Anthes, 1971). This result may be ascribed to some modeling problems such as the

formulation of the effect of moist convection, the lack of convective transport of momentum, the lack of radiational effects, etc. Non-existence of large-scale basic flow in the present model should be noted, too. As suggested in the analysis of actual hurricanes made by Black and Anthes, mean basic flow may interact

with a hurricane vortex to establish a particular dynamical structure. Yamasaki (1969) suggested a considerable change of structure under the existence of vertical wind shear.

The mean vertical flow is upward throughout the troposphere within a radius of about 140 km. The bottom left part of Fig. 10 shows that such an area is surrounded by a region of downward motion with less intensity than the upward motion by an order of magnitude. Beyond about 300 km radius, $\bar{\omega}$ becomes weak and its distribution pattern is not well organized.

The distribution of the standard deviation for each component of flow is shown in the right half of Fig. 10. Except for the small upper central region, $SD(v_\theta)$ is much smaller than $\bar{v}_\theta$. It is also seen that $SD(v_r)$ is generally slightly larger than $SD(v_\theta)$, yet it is considerably smaller compared to $\bar{v}_\theta$ and/or $\bar{v}_r$ except in the upper outflow layer. Accordingly, the wind vector distribution at the middle and lower levels should appear to be almost symmetric. Both $SD(v_\theta)$ and $SD(v_r)$ are large in the region where the upper level flow $\bar{v}_r$ is large. The flow field at level 2 clearly exhibits an asymmetric feature, as will be shown in the next subsection.

The vertical motion in the central region is generally upward, although beyond a radius of 100 km, it is upward at some sections and downward at others; thus, $SD(\omega)$ can become larger than the magnitude of $\bar{\omega}$.

d. Asymmetric features

Before discussing the asymmetric features of a simulated tropical cyclone at the mature stage, statistics showing the development of azimuthal perturbations are presented. In Table 4, the average standard deviation for the radius-height (sigma) domain within 500 km radius is listed for various quantities at 10-hr intervals. As the variation of annular length with radius is not considered in taking the average, the computed result differs from the area or space average. In Table 4, very small values of SD at Hour 0 are caused by the scheme for interpolating the grid point values onto 40 equally spaced points on each radius circle. The increase in the average SD is especially noticeable for three periods, i.e., Hours 10 to 20, Hours 40 to 50 and Hours 70 to 90. After the third period, the average SD of each quantity fluctuates around a certain value.

The azimuthal perturbation, which will be denoted by primes, may be defined as a deviation of a quantity from its azimuthal average. Fig. 11 shows the distribution of ω', T' and QCON' on the cylindrical surface at 60 km radius, where many quantities have large SD's. As mentioned before, QCON is the heat source due to condensation and convection processes. The figure for ω' shows two narrow areas of large negative value extending vertically through the whole troposphere. In between these two areas, there exists a broad area of relatively small positive value. Note that the total

TABLE 4. Time variation of average standard deviation for p_*, θ_e, T, v_θ, v_r and ω. The average is taken for the radius-sigma domain within 500 km radius.

Hour	p_* (mb)	θ_e (°K)	T (°K)	v_θ (m sec^{-1})	v_r (m sec^{-1})	ω (10^{-3} mb sec^{-1})
0	0.005	0.00	0.001	0.00	0.00	0.00
10	0.011	0.06	0.009	0.03	0.03	0.15
20	0.135	0.65	0.152	0.70	0.71	3.90
30	0.110	0.74	0.142	0.77	0.84	2.08
40	0.163	0.88	0.184	0.91	1.13	3.47
50	0.360	1.02	0.303	1.59	1.82	5.06
60	0.443	1.16	0.364	1.65	2.25	5.63
70	0.331	1.02	0.387	1.46	1.99	6.15
80	0.617	1.15	0.471	1.76	2.61	6.58
90	0.569	1.31	0.535	2.21	3.18	8.28
100	0.489	1.29	0.570	2.00	2.69	8.85
110	0.353	1.28	0.542	2.04	2.76	7.79
120	0.414	1.27	0.458	1.97	2.47	7.57
130	0.467	1.10	0.409	1.62	2.44	6.28
140	0.794	1.21	0.516	1.87	2.91	8.40
150	0.696	1.19	0.475	1.90	2.75	7.85
160	0.407	1.13	0.480	1.76	2.41	7.10

vertical motion at this radius is mostly upward as $\bar{\omega}$ is negative and of the same order of magnitude as that of maximum ω'. For example, the value of $\bar{\omega}$ at this moment at level 5 is -34 in the same units as that for ω', which ranges from -155 to 53. In addition to the main mode mentioned above, a higher order mode is seen at the upper levels. The general features of the QCON' pattern are quite similar to those of ω'. In the units for QCON' in Fig. 11, $\overline{QCON}$ at level 5 is 2.75. Of course, QCON itself is non-negative.

The features of the T' distribution differ from those of ω'. Roughly speaking, the lowest mode, i.e., one positive and one negative section, is predominant in the middle troposphere and also in the lower levels but with the opposite phase. In the upper troposphere, the mode of the smaller scale develops so that three or four maxima appear.

Comparing the distributions of ω', T' and QCON', a discussion on the energetics may be made as follows. In the upper and middle troposphere, negative ω', which means relative adiabatic cooling, and the heating represented by QCON' are observed where T' is positive. In other words, the azimuthal variation of T tends to be destroyed by ω' and to be amplified by QCON'. The negative correlation between T' and ω' means that the total potential energy is released by baroclinic process. The role of ω' and QCON' on the change of T' field is reversed in the lower troposphere. The relatively warm section is maintained by the adiabatic warming or relatively less cooling due to the vertical motion of positive ω'.

At Hour 151, the total baroclinic effect integrated for the column space of 500 km radius is to release the total potential energy at the mean rate of 0.44×10^4 ergs cm^{-2} sec^{-1}. At the same time, the mean rate of work done to the column through the boundary at 500 km radius is -0.05 in the same units. The sum of the
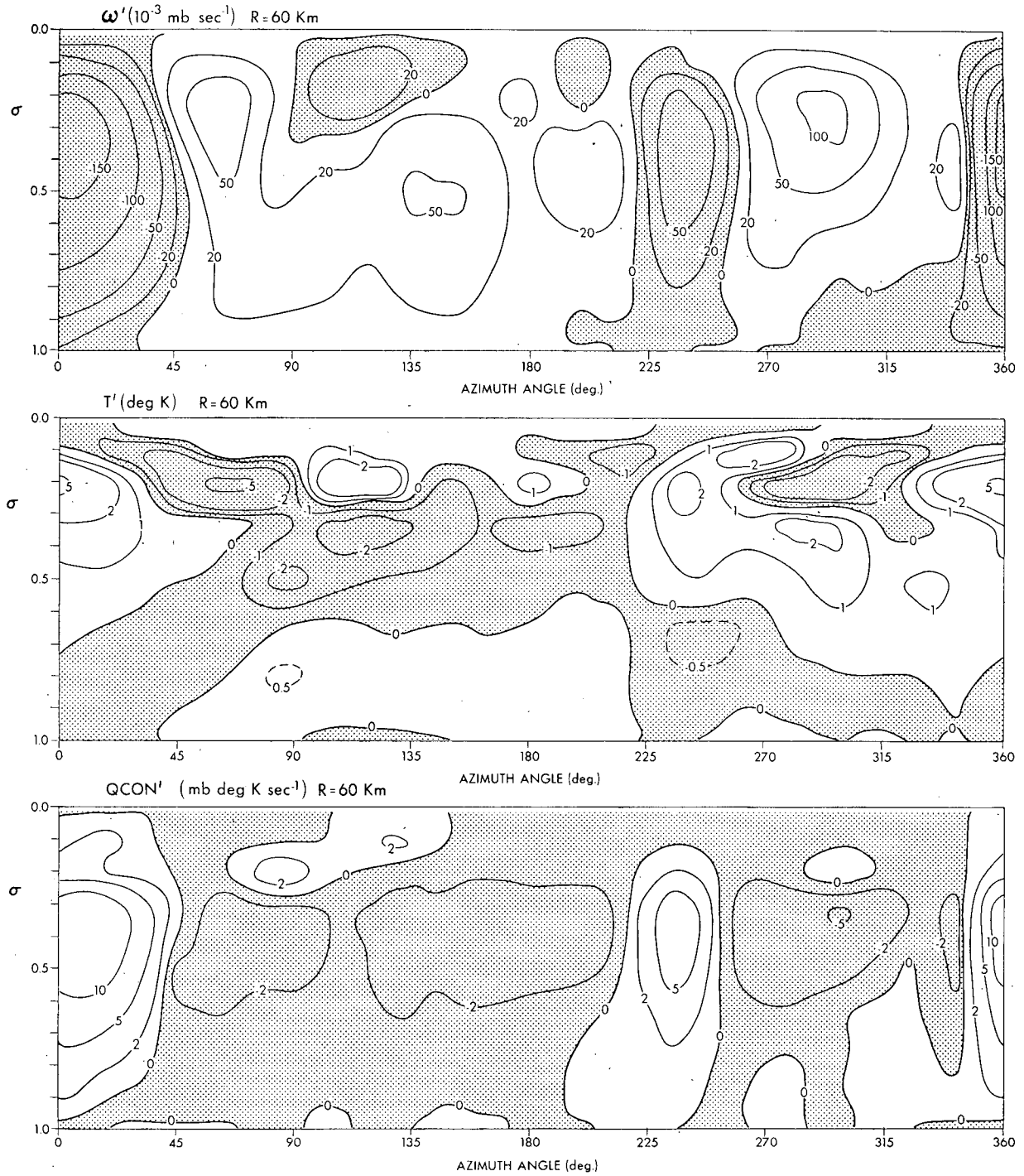
FIG. 11. Distribution of azimuthal perturbation ω' (top), T' (middle) and QCON' (bottom), on the cylindrical surface at 60 km radius.

above two effects gives the generation rate of the eddy kinetic energy k_E, locally defined as $\bar{v}_\theta v_\theta' + \bar{v}_r v_r' + (v_\theta' v_\theta' + v_r' v_r')/2$. On the other hand, the barotropic process, which is associated with the eddy transport of momentum, gives the conversion of the kinetic energy of the azimuthal mean flow to k_E. In Table 5, the mean

generation and the barotropic conversion are listed together with the dissipation of k_E and the inflow of k_E through the open boundary at 500 km radius. The energy source for k_E is both the barotropic conversion and the generation which is primarily due to the baroclinic process. It is noted here that the mean eddy

kinetic energy within 500 km radius at Hour 151 is 7.63 J cm^{-2}, which is approximately 1/20 the energy for the mean flow, i.e., 153 J cm^{-2}. The budget of the eddy kinetic energy discussed above is different from the results of Anthes (1972), which indicates that the energy source is solely due to conversion by the barotropic process.

The horizontal eddy motion is predominant at the upper levels as has already been seen in the distribution of SD(v_θ) and SD(v_r). Fig. 12 shows the field of horizontal wind vectors at levels 2, 5 and 11. The asymmetric component at levels 5 and 11 is so small compared to the azimuthal mean that the field appears to be almost symmetric. At level 2, the uneven four branches of flow are seen going out from the central cyclonic flow region. Any resemblance of this field to that of actual hurricanes (e.g., Hawkins and Rubsam, 1968; Yanai, 1968; Black and Anthes, 1971) is weak. In the actual case, the field is established in the context of the large-scale basic flow. As noted before, such a basic flow is not present in this model. The distribution of mass divergence at upper levels is not symmetric, although this may well be related to the slow movement of the pressure center in the present experiment.

e. Eye-like structure

In numerical experiments on tropical cyclones, a few models have yielded a distinct region of subsidence at the storm center (e.g., Rosenthal, 1971), while others have no such feature or, if any, a weak sinking layer of small depth and short duration.

It should be admitted that the horizontal resolution of 20 km, the finest in the present model, is not adequate for the simulation of the detailed structure near the center. In this experiment, a structure like the eye of a tropical cyclone appears and lasts with varying intensity during the development period. At the mature stage, it tends to lose its deep penetrative nature and sometimes becomes obscure. At Hour 151, it is observed at about 30 km to the right of the storm center, i.e., the pressure center. A vertical cross section, which passes both the pressure center and the eye, is shown for θ_e, r and ω, in Fig. 13.

A relatively low equivalent potential temperature at the middle level in a barely resolved eye is largely due

TABLE 5. Budget of eddy kinetic energy (units, 10^4 ergs cm^{-2} sec^{-1}) for the column domain of 500 km radius at Hour 151.

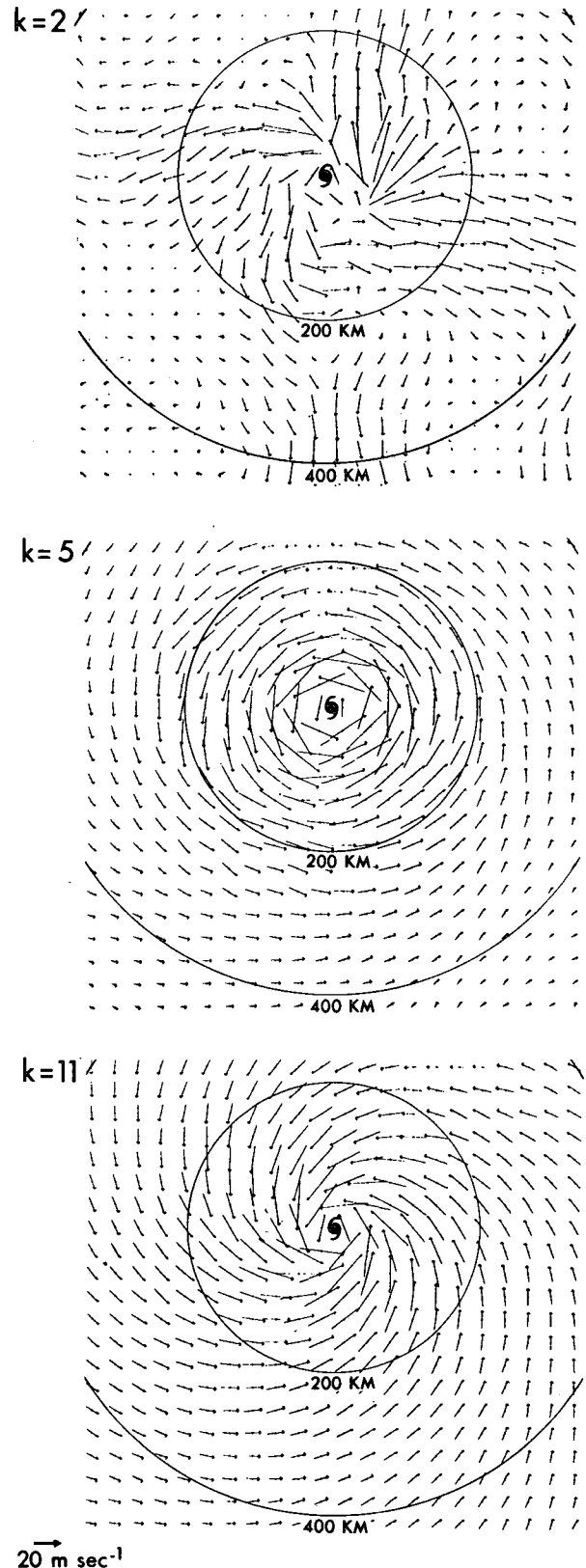| Components	
Generation of k_E	0.39
Conversion of the energy of mean flow (barotropic process)	0.56
Dissipation due to momentum diffusion	
Horizontal diffusion	−0.71
Vertical diffusion	−0.04
Inflow of k_E	
By symmetric flow	−0.09
By asymmetric flow	−0.08

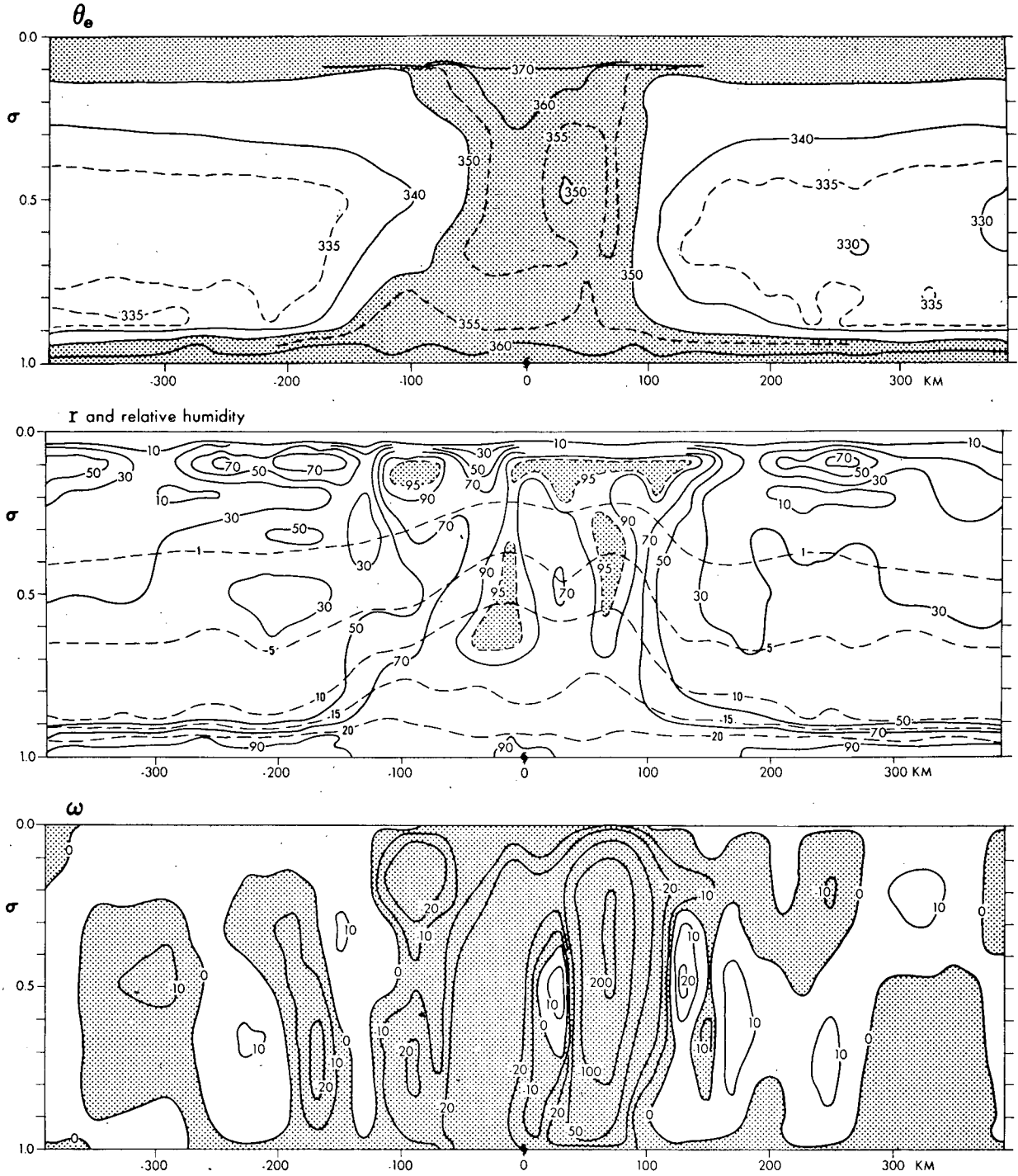FIG. 12. Distribution of horizontal wind vectors at levels 2, 5 and 11, at Hour 151.

FIG. 13. Vertical cross section through the pressure center and the eye, at Hour 151, for θ_e (top, °K), r (middle, dashed line, gm kg^{-1}), relative humidity (middle, solid line, percent) and ω (bottom, 10^{-3} mb sec^{-1}). Areas with $\theta_e > 350$K, relative humidity $>95\%$ and $\omega < 0$ are shaded.

to the dryness of the air. This relatively dry area coincides with a small area of downward motion within a region of strong upward motion. For the range from -50 to 90 km in Fig. 13, the initial conditionally unstable state is almost neutralized to establish a warm

moist core and upward motion is observed throughout the troposphere. Such a region may be called an eyewall region. In the outer area, a nodal vertical distribution of ω is seen. At about -250 km and 320 km, a small increase of mixing ratio at the lower level is
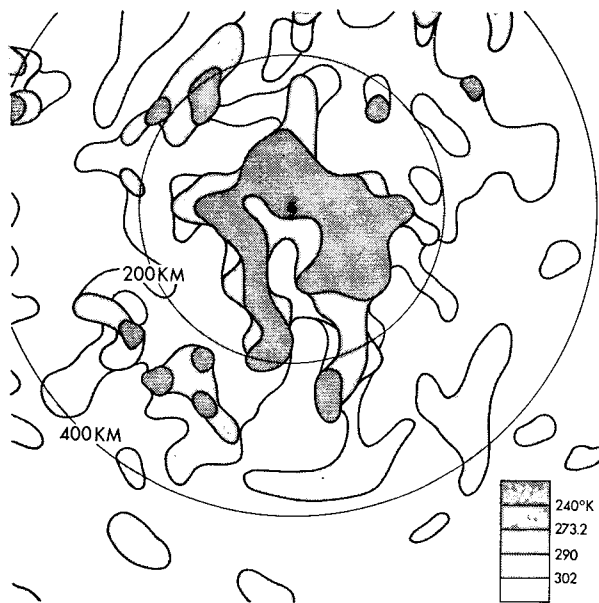
FIG. 14. Distribution of temperature at cloud top at Hour 151. Unshaded area is without cloud.
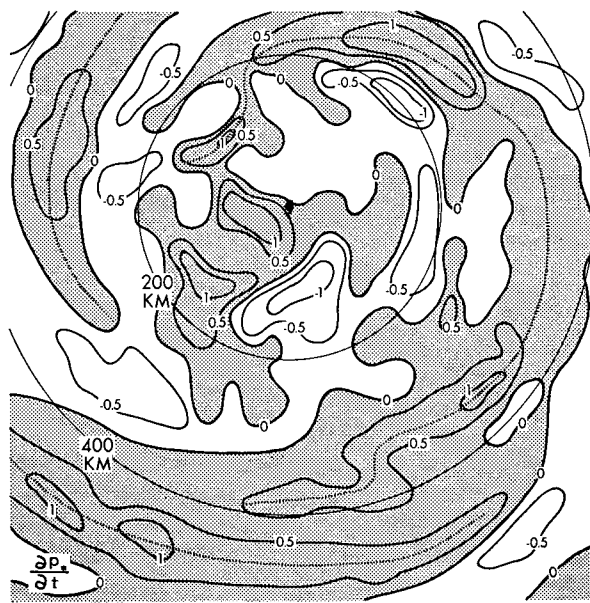
FIG. 15. Distribution of surface pressure tendency (10^{-3} mb sec^{-1}) at Hour 151. The area with positive tendency is shaded. Dotted lines represent the center of spiral band.

observed. This is related to the band structure to be discussed in the next section.

The eye mentioned above is about 30 km off the storm center. It may be of interest to see the distribution of clouds at this moment, i.e., Hour 151. The level of cloud top is defined as the highest level where the condensation and convective heating is evaluated, i.e., QCON>0. Fig. 14 shows the temperature distribution with low temperatures meaning high cloud tops. It is seen that a high cloud wall nearly encircles an area where clouds do not reach the freezing level. The position of such area is about 70 km off the pressure center

and does not coincide with that of the eye. The clouds in the outer area are generally shallow. The high cloud tops outside of the cloud annulus do not imply penetrative tall clouds but thin clouds in the upper layers.

6. Spiral bands in a model tropical cyclone

Spiral bands are a common feature in the distribution of clouds and radar echoes in actual tropical cyclones.

The analysis of the bands as observed on radar indicates that they propagate radially outward (e.g., Senn and Hiser, 1959). At the passage of a band, a
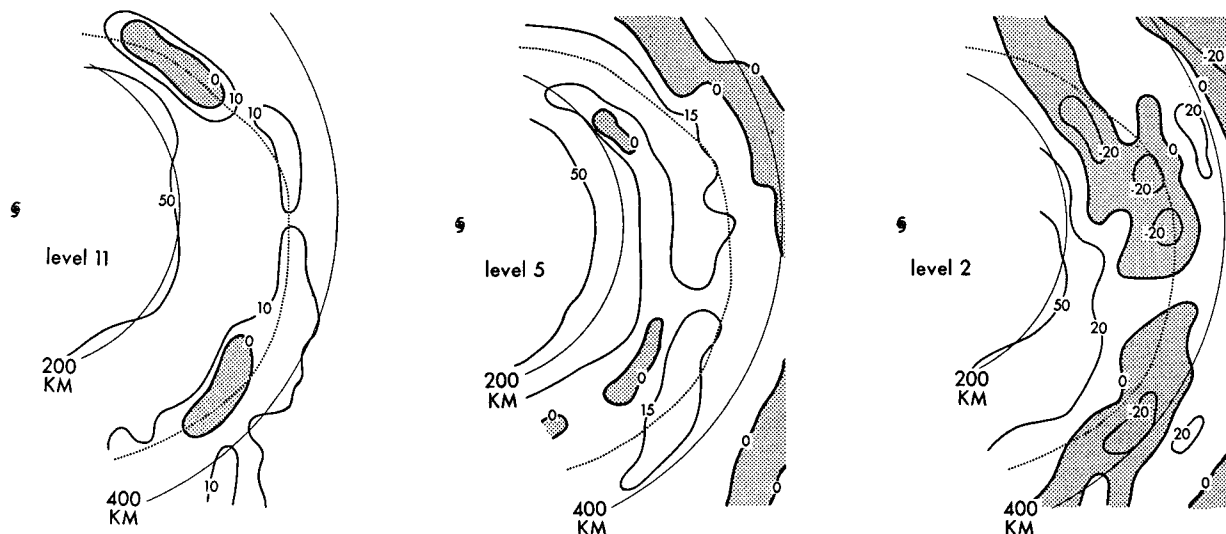
FIG. 16. Distribution of the inward component of pressure gradient force (10^{-2} cm sec^{-2}) at levels 11 (a), 5 (b) and 2 (c), at Hour 151. Dotted line indicates the center of band. Negative values are shaded.
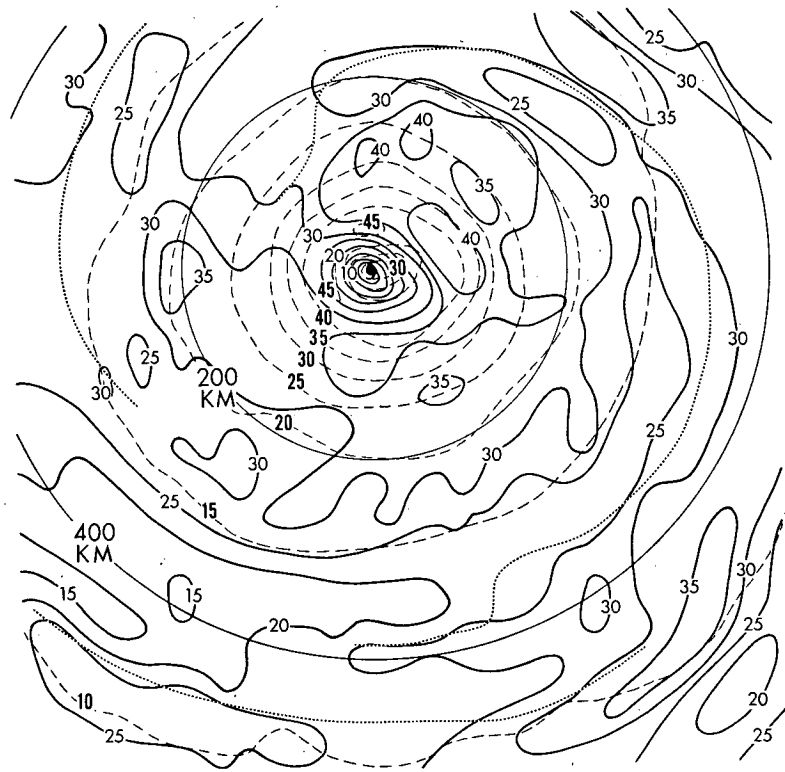
FIG. 17. Distribution of wind speed (dashed lines, m sec^{-1}) and inflow angle (solid lines, deg) at level 11, at Hour 151. Dotted line indicates the center of band.

specific change in surface meteorological quantities is observed (Wexler, 1947; Lidga, 1955; Ushijima, 1958; Tatehira, 1961, 1962). It seems almost certain that passage of a band is accompanied by a corre-sponding drop and rise of the surface pressure; by a wind shift indicating low-level convergence and upward motion; and by a temperature drop. Variation of D-value, which means undulation of an isobaric surface,
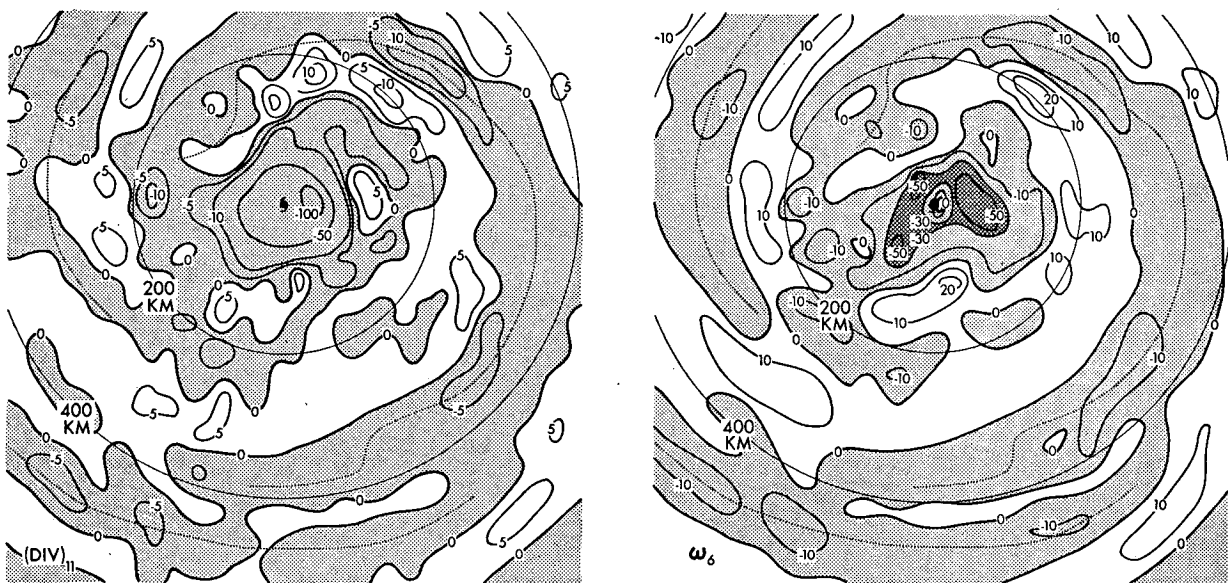
FIG. 18. Distribution of divergence of wind at level 11 (left, 10^{-5} sec^{-1}), and ω at level 6 (right, 10^{-3} mb sec^{-1}), at Hour 151. Areas of convergence and negative ω are shaded. Center of band is indicated by dotted line.
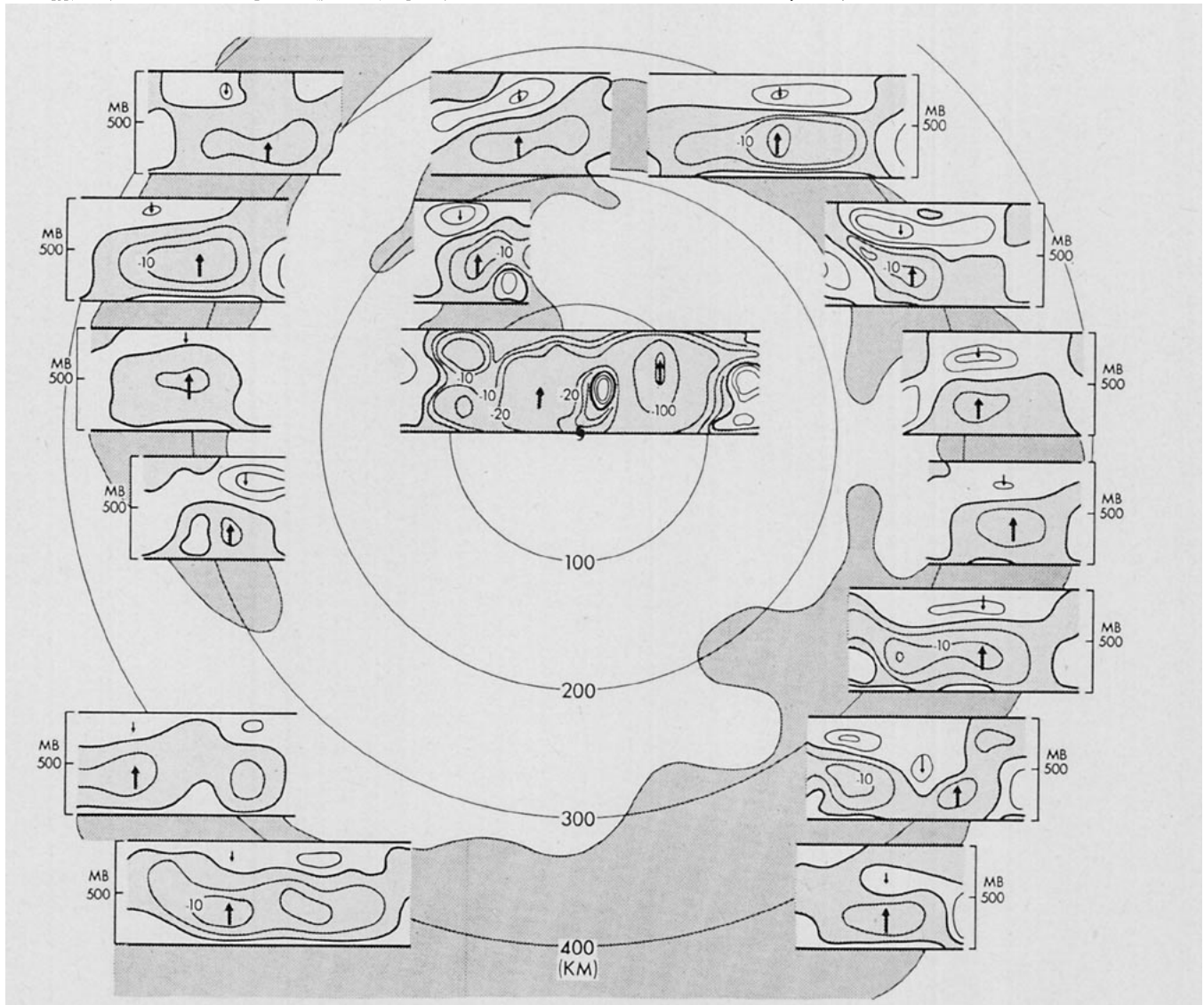
Fig. 19. Vertical cross section of ω at Hour 151 along the band, i.e., dark shaded area. The base line of each cross section indicates the position of the vertical section. In the cross sections, areas with negative ω are lightly shaded and contour lines are drawn every 5×10^{-3} mb sec^{-1}. Maximum negative and positive value of ω are indicated by the heavy and light arrows, respectively.

has been observed by reconnaissance flights crossing a band (e.g., Simpson, 1954).

It has been shown that a band or zone structure of a typhoon may be analyzed by studying the fluctuating field of precipitation and surface pressure (Staff members, Tokyo University, 1969). Upper level analysis also suggests a banded structure, despite the limited observations (e.g., Masuda and Takeuchi, 1951, and Hawkins and Rubsam, 1968).

Provided that a simulated tropical cyclone in a model is fairly realistic, the model may be also regarded as a good simulation of a dense three-dimensional network of simultaneous observations.

a. Structure of a spiral band

In the present experiment, it was found that the surface pressure tendency is an appropriate quantity

for detecting spiral bands in a tropical cyclone at the mature stage. Fig. 15 shows the distribution of the tendency of p_* at Hour 151. In this figure, the areas of positive tendency, i.e., the spirally shaded areas, may be defined as spiral bands. The rainfall observed around these bands forms a kind of spiral rain band. Note, however, that these pressure-tendency bands stretch much longer than the rain bands and many portions of the bands are without precipitation. The widths of the bands are approximately 100 km. The dotted lines in Fig. 15 represent the center lines of the bands which trace the places of maximum tendency. Note that Fig. 15 only covers an area of 800 km$\times$800 km, a very small portion of the whole integration domain, 4000 km$\times$4000 km.

It will be shown later that these pressure-tendency bands move outward. The outward movement of the
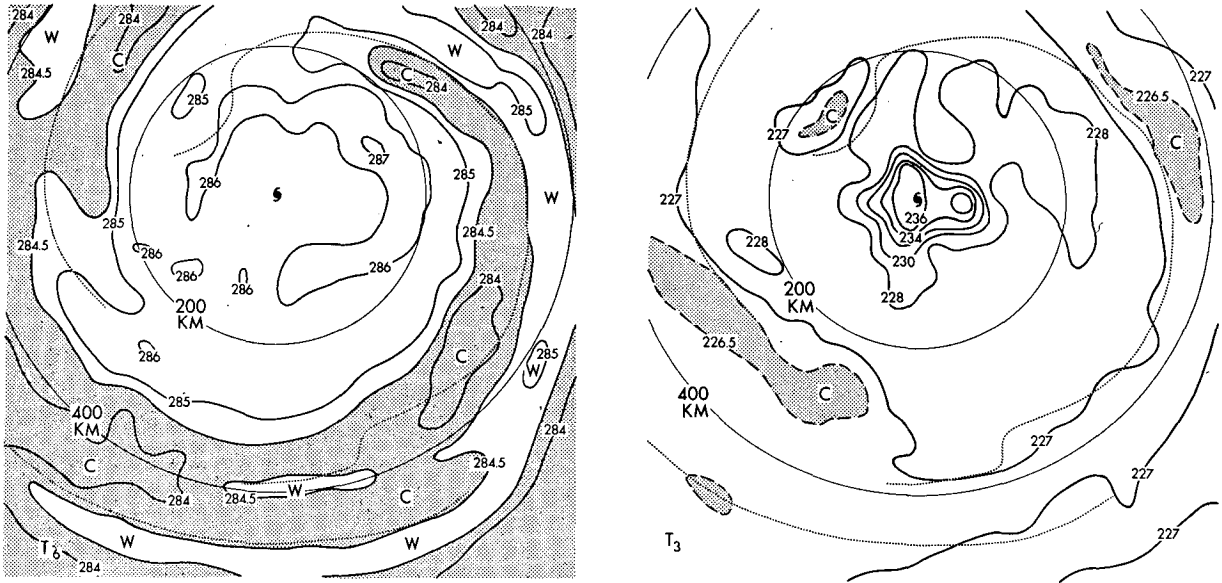
FIG. 20. Distribution of temperature at levels 6 and 3, at Hour 151. Areas with temperatures below 284.5K and 226.5K, respectively, are shaded. The dotted line indicates the center of band.

surface pressure tendency as shown in Fig. 15 suggests the existence of a high and low pressure system along the rear and the front edge of the band, respectively. If so, the inward component of the pressure gradient force should be relatively small along the band center. This feature is seen in Fig. 16a, which shows the distribution of the inward component of the pressure gradient force at the lowest level. The range of pressure variation across the band is estimated to be of the order of 1 mb. Similar analyses for levels 5 and 2 are shown in Figs. 16b and c. These figures imply a high pressure system is

along the front edge of the band at level 5, while it is along the rear edge at level 2 and at the lowest level.

The wind field is examined next. Fig. 17 shows the distribution of speed and inflow angle of the wind at level 11. The wind speed does not show a significant change across the band, while the wind direction does. The inflow angle in the front part of the band is larger than that in the rear by 10°–20°. This is reflected in the left part of Fig. 18 showing the distribution of divergence at level 11. The zone of convergence coincides with the band. The magnitude is about 5×10^{-5}
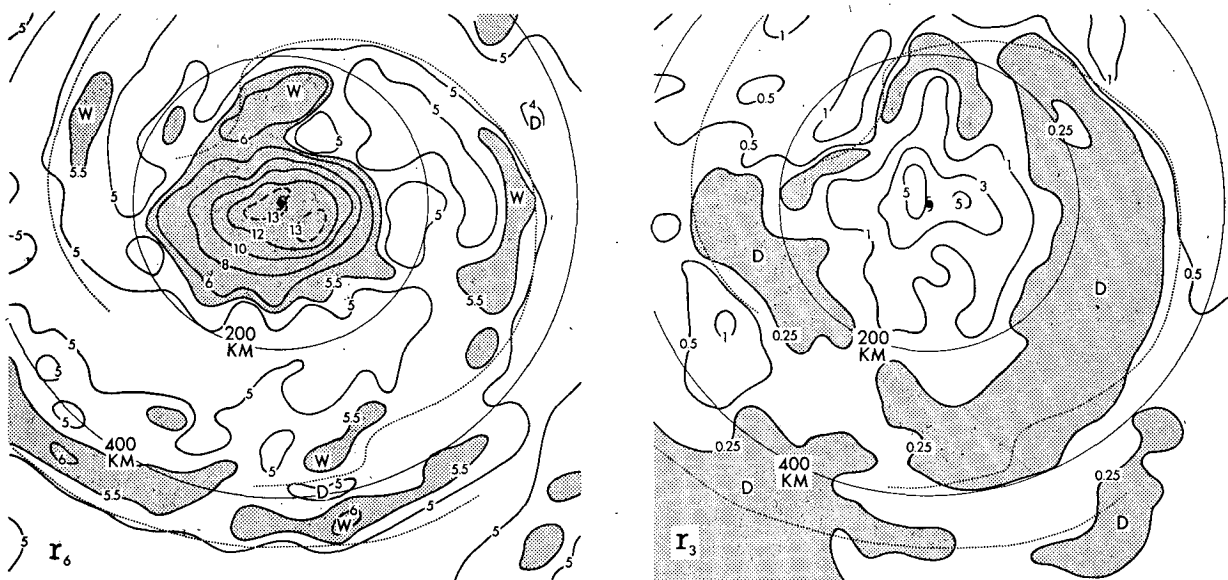

FIG. 21. Distribution of mixing ratio at levels 6 and 3 at Hour 151. Areas with mixing ratios greater than 5.5 and less than 0.25 gm kg^{-1}, respectively, are shaded. The dotted line indicates the center of the band.
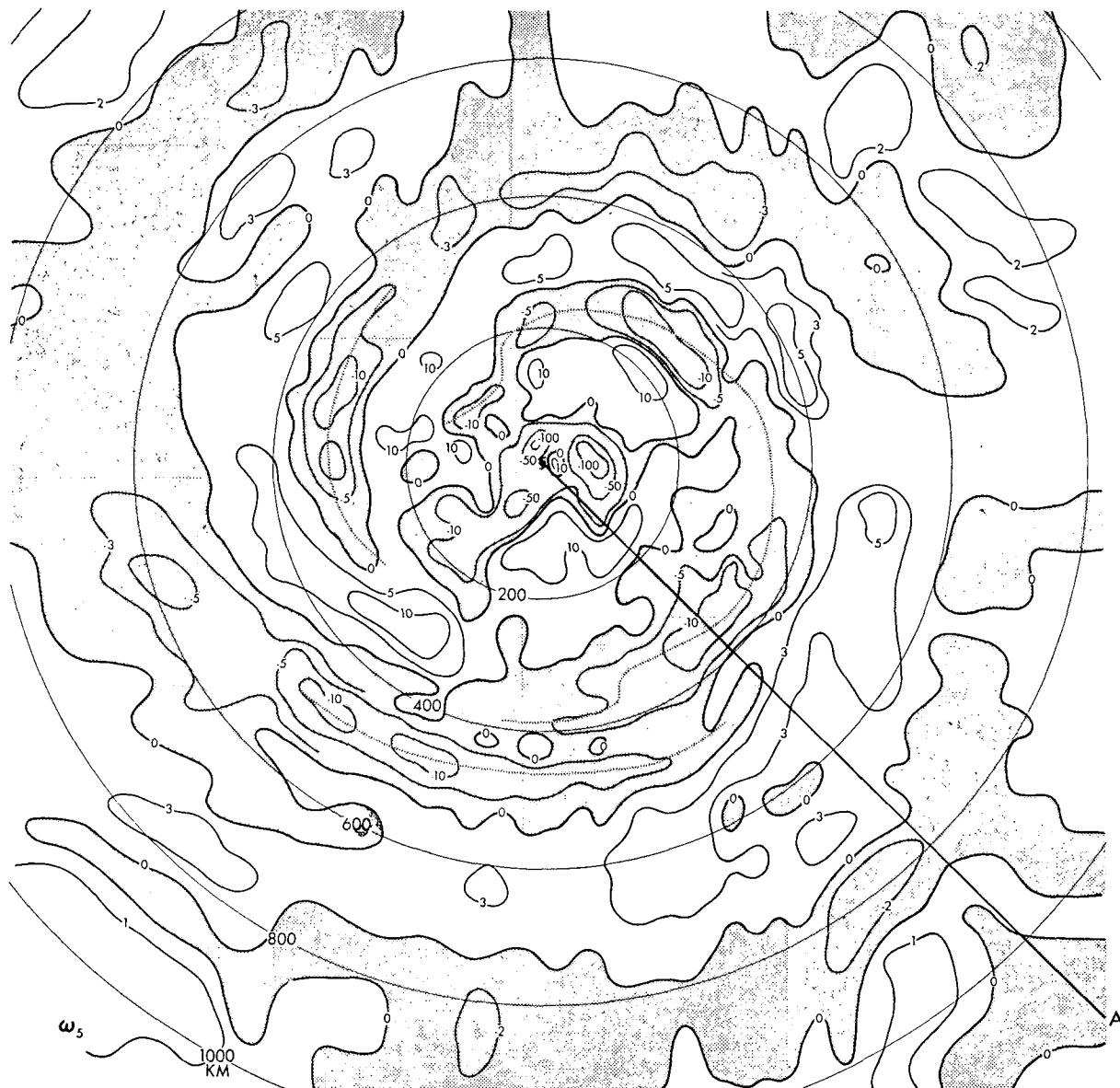
FIG. 22. Distribution of ω (10^{-3} mb sec^{-1}) at level 5 at Hour 151. Areas with negative values are shaded.

sec^{-1}. At level 5, a zone of divergence with the same magnitude appears along the band (figure not shown). It becomes a convergence zone again at level 2. The field of vorticity does not exhibit such a clear-cut association with the band.

The above-mentioned horizontal wind field implies upward motion along the band at least in the lower troposphere. The right part of Fig. 18 shows clearly the in-phase relation between ω at level 6 (i.e., at about 660-mb level) and the band. In order to see the vertical variation of ω, cross sections of ω taken at various portions along the band are shown in Fig. 19. The base line of the cross section indicates the position of the vertical sections. Note that the existence of a node or change of direction of vertical motion is a general fea-

ture, i.e., the flow is downward at the higher levels above the band. A small positive value of ω near the bottom in many sections is due to a positive surface pressure tendency and does not mean downward motion. Within about 100 km from the center, strong upward motion is observed at all levels except for the downward flow in the eye. Fig. 20 shows the distribution of temperature at levels 6 and 3. The field of mixing ratio is also presented in Fig. 21. In the lower troposphere, the front part of the band is relatively warm and dry, while the rear part is cold and moist. The status in the upper troposphere is opposite to that in the lower levels. The band structure of the temperature field is hydrostatically consistent with the field of pressure discussed before.
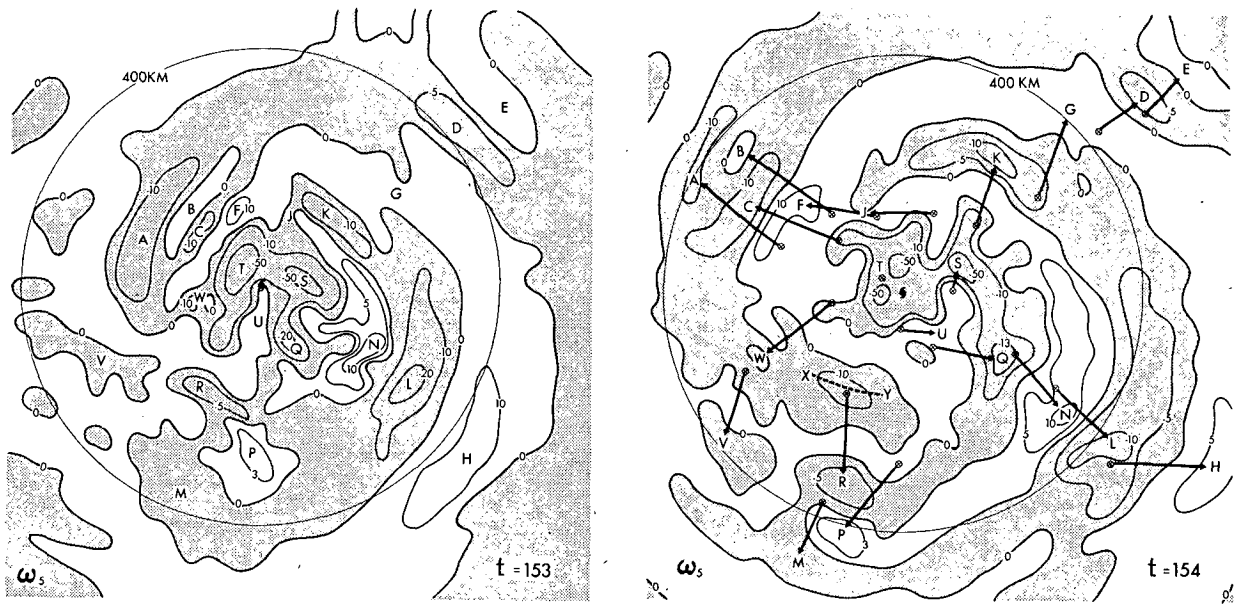
FIG. 23. Distribution of ω (10^{-3} mb sec^{-1}) at level 5 at Hours 153 and 154. The letters A, B, C, etc., are used
for the identification of the pattern.

b. Movement of spiral bands

In order to investigate the movement of the bands, the map of ω at level 5 is drawn every hour for the larger domain, i.e., 1600 km×1600 km. Fig. 22 is such a map for Hour 151. Spiral bands are seen to extend beyond 800 km with weakening vertical motion. A disturbed field can be easily identified, if the field is separated into the azimuthal average at each radius and the deviation from it. In the present case, however, the azimuthal average of ω is one order of magnitude smaller than ω itself except for the region within about 100 km. Hence, the map of ω itself has been prepared.

A band may be traced by examining the movement of the distribution pattern of ω. For example, Fig. 23 shows the movement of the pattern from Hours 153 to 154. The letters A, B, C, etc., are used for the configurational identification. It is seen from Fig. 23 that the bands propagate radially outward. Circular move-
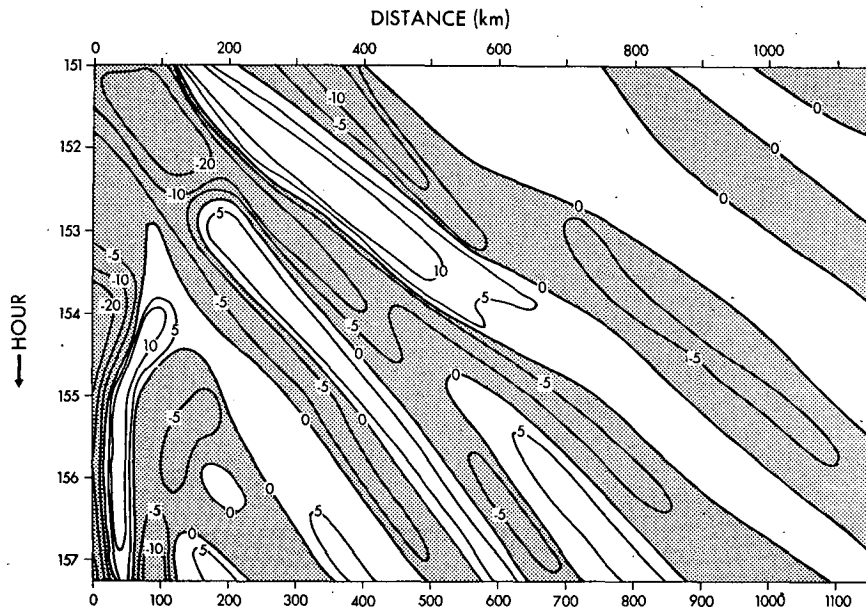

FIG. 24. Time-radius section of ω (10^{-3} mb sec^{-1}) at level 5. Portions with negative values
are shaded. The radius is along line A in Fig. 22.

ment may exist near the center, but very little else-where. In Fig. 24, the time series of vertical velocity with alternating sign along a radial line A in Fig. 22 is presented. The speed of propagation of the bands is approximately 100 km hr^{-1}. It may be of interest to note that the cellular structure which is quite similar to the band in the present model appeared in the axisymmetric model, too, and these annuluses moved outward.

If the band moves radially outward, a portion of the spiral near the center should have existed for a shorter period than part in the outer domain. For example, the part X-Y of the band at Hour 154 in Fig. 23 does not have a corresponding portion at Hour 153. Thus, that part apparently formed during Hours 153 and 154. Such an analysis can be made over an extended period by preparing a composite map of a band. Fig. 25 shows one example. It appears that a source point of the spiral band is in a region surrounding the center. A source appears to move cyclonically while producing a new portion of band. Other bands examined showed similar behavior.

The rainfall distribution is also shown in Fig. 25. In the present case, the precipitation observed within the band is generally small. It seems that rainfall in the outer region is not of primary importance in the present model for the maintenance and propagation of a band.

c. Summary of analysis and remarks

The structure of bands analyzed in the preceding two subsections is summarized in Fig. 26. The pressure and wind fields near the surface are in good agreement with actual observations (e.g., Tatehira, 1962). The present analysis also revealed the upper level structure
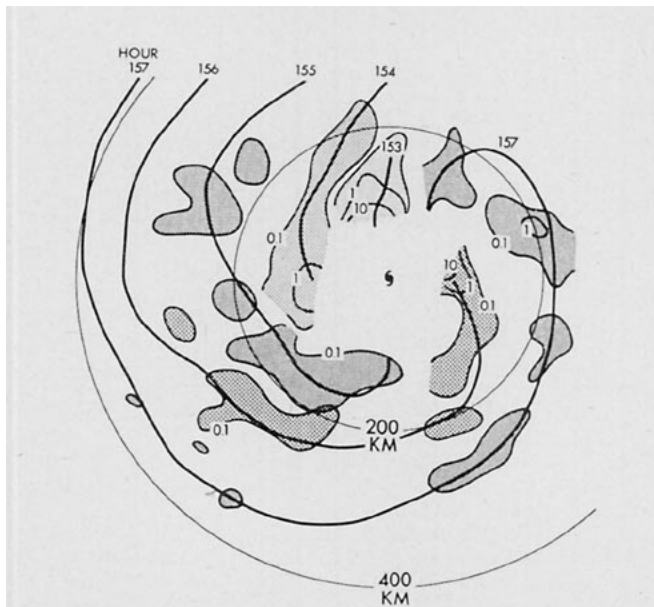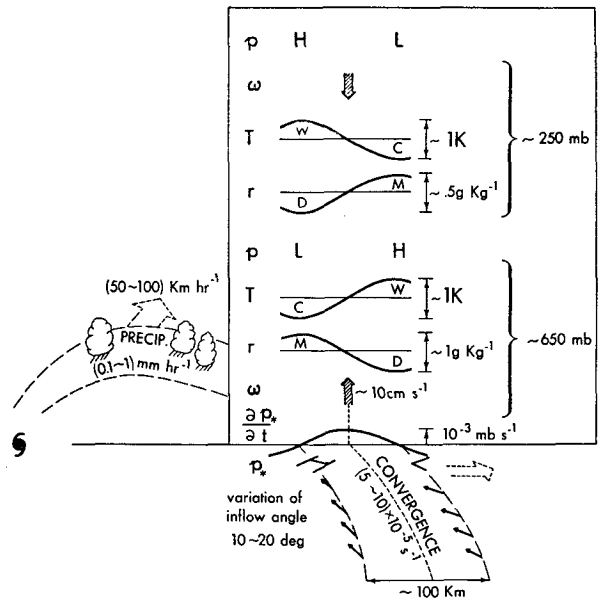

Fig. 26. Schematic diagram showing the results of the analysis.

which has not been previously presented because of sparse observation. The band in the present model moves radially outward. This agrees with the result of rain band analyses (e.g., Senn and Hiser, 1959).

In simulation experiments of a tropical cyclone, spiral bands were obtained in the numerical model by Anthes et al. (1971) and also in the model by Anthes (1972). However, the characteristics of the band in those models were different in some respects from what has been analyzed in the present model. Their bands have a long life span and rotate cyclonically about the storm center while they propagate outward. Uniformity in the temperature field has also been mentioned.

Diagnosis of the bands obtained in the present model leads to the speculation that the bands behave like internal gravity waves. Suppose that an internal gravity wave propagates in the x direction in a stably (in dry sense) stratified fluid. The linearized equations for this system may be written in pressure coordinates as

$$\left.\begin{array}{c} \dfrac{\partial u}{\partial t} = -\dfrac{\partial \phi}{\partial x} \\[2mm] \dfrac{\partial}{\partial t}\left(\dfrac{\partial \phi}{\partial p}\right) = -S\omega \\[2mm] \dfrac{\partial u}{\partial x} + \dfrac{\partial \omega}{\partial p} = 0 \end{array}\right\},$$

where u is the velocity in x direction, ϕ the geopotential of an isobaric surface, S the static stability parameter [i.e., $S=(\partial\phi/\partial p)(\partial \ln\theta/\partial p)$], ϕ and θ are the geopotential and potential temperature of the basic field,

Fig. 25. Composite map of a band. Areas of rainfall with intensity greater than 0.1 mm hr^{-1} are shown by shading along bands.
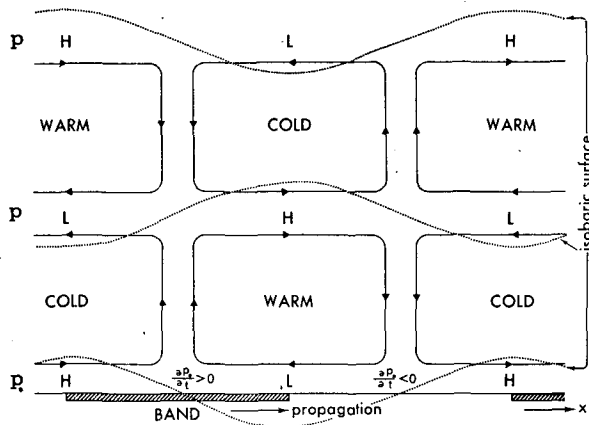
FIG. 27. Schematic diagram showing a typical structure of an internal gravity wave which may represent the band. Note that the mean hurricane field is not included.

respectively, and $\omega = dp/dt$. The phase relationship among the quantities of the above system is that ω is ahead of $-\partial\phi/\partial p$ or temperature by 90°; ϕ is behind the horizontal convergence $-\partial u/\partial x$ by 90°; and u and ϕ are in phase. The phase speed of the wave is given by $S^{\frac{1}{2}}P/(2\pi)$ where P is the vertical pressure scale of the wave. For a typical value of S for the present model, i.e., $S = 3.5 \times 10^{-2}$ m^2 sec^{-2} mb^{-2}, and $P = 900$ mb, which corresponds to vertical wavenumber 1, the phase speed becomes 96 km hr^{-1}. The wave of this mode is illustrated in Fig. 27. The structure and the speed of the bands obtained in the model are in good agreement with those of the gravity wave discussed above.

It is also noted from the phase relationship that the correlation between ω and T is zero while that of u and ϕ is positive. Accordingly, the baroclinic conversion of energy does not take place in the band and the pressure work acts outward through the moving band. An energy conversion may occur, however, if the temperature field should be shifted as a result of the increase in the rainfall intensity along the band. The pressure work mentioned above is very small as compared to the pressure work in the opposite direction due to the basic flow. Thus, its energetical contribution to the whole system is small. The zero correlation between u and ω, meaning no vertical propagation of momentum in the band, suggests that there is no kinetic energy conversion between the band system and the mean basic flow with vertical shear. It seems that, once the band is formed, it propagates outward without appreciable further supply of energy, as far as the present case is concerned.

The problems which are put aside for future study are the generation of bands, the selection of horizontal and vertical scales, etc. A hint suggested from the present analysis is that a new portion of a band may be formed in the region surrounding the storm center by a cyclonically moving source point. This feature apparently agrees with the radar echo analysis made by Senn and Hiser (1959).

7. Remarks

The present simulation experiment demonstrates the capability of the three-dimensional tropical cyclone model in the following subject areas:

1) Development of a large weak vortex into a strong hurricane-like vortex
2) Maintenance of a strong vortex, without disintegration under the development of asymmetry
3) Simulation of the band structure in the outer region of a storm.

In future experiments, the constraints imposed on the present model should be removed in order to improve the model's capability so that the problems in the whole life cycle of a tropical cyclone can be treated more realistically. An improvement of the model along this line is being undertaken.

It is also important to refine the physics of the model. For example, the effect of radiation and the response of the ocean to a storm should be considered. An improved or new scheme for parameterization of the sub-grid-scale processes is urgently needed.

REFERENCES

Anthes, R. A., 1972: Development of asymmetries in a three-dimensional numerical model of the tropical cyclone. *Mon. Wea. Rev.*, **100**, 461–476.

——, S. L. Rosenthal and J. W. Trout, 1971: Preliminary results from an asymmetric model of the tropical cyclone. *Mon. Wea. Rev.*, **99**, 744–758.

Arakawa, A., 1971: A parameterization of cumulus convection and its application to numerical simulation of the tropical general circulation. Paper presented at the 7th Tech. Conf. on Hurricanes and Tropical Meteorology, Barbados, Amer. Meteor. Soc.

Benwell, G. R. R., and F. H. Bushby, 1970: A case study of frontal behavior using a 10-level primitive equation model. *Quart. J. Roy. Meteor. Soc.*, **96**, 287–296.

Black, P. G., and R. A. Anthes, 1971: On the asymmetric structure of the tropical cyclone outflow layer. *J. Atmos. Sci.*, **28**, 1348–1366.

Delsol, F., K. Miyakoda and R. H. Clarke, 1971: Parameterized processes in the surface boundary layer of an atmospheric circulation model. *Quart. J. Roy. Meteor. Soc.*, **97**, 181–208.

Ellison, T. H., 1957: Turbulent transport of heat and momentum from an infinite rough plane. *J. Fluid Mech.*, **2**, 456–466.

Hawkins, H. F., and D. T. Rubsam, 1968: Hurricane Hilda, 1964:

Structure and budgets of the hurricane on October 1, 1964. *Mon. Wea. Rev.*, **96**, 617–636.

Holloway, J. L., and S. Manabe, 1971: Simulation of climate by a global circulation model, 1. Hydrologic cycle and heat balance. *Mon. Wea. Rev.*, **99**, 335–370.

Koteswaram, P., 1967: On the structure of hurricanes in the upper troposphere and lower stratosphere. *Mon. Wea. Rev.*, **95**, 541–564.

Kurihara, Y., 1965: On the use of implicit and iterative methods for the time integration of the wave equation. *Mon. Wea. Rev.*, **93**, 33–46.

——, 1968: Note on finite difference expressions for the hydrostatic relation and pressure gradient force. *Mon. Wea. Rev.*, **96**, 654–656.

——, 1973: A scheme of moist convective adjustment. *Mon. Wea. Rev.*, **101**, 547–553.

——, and J. L. Holloway, 1967: Numerical integration of a nine-level global primitive equations model formulated by the box method. *Mon. Wea. Rev.*, **95**, 509–530.

Ligda, M. G. H., 1955: Hurricane squall lines. *Bull. Amer. Meteor. Soc.*, **36**, 340–342.

Manabe, S., J. Smagorinsky and R. F. Strickler, 1965: Simulated climatology of a general circulation model with a hydrologic cycle. *Mon. Wea. Rev.*, **93**, 769–798.

——, J. L. Holloway, Jr., and H. M. Stone, 1970: Tropical circulation in a time-integration of a global model of the atmosphere. *J. Atmos. Sci.*, **27**, 580–613.

Masuda, Y., and M. Takeuchi, 1951: An aerological investigation of the structure of typhoon—Analyses of the typhoon Jane and Kezia. *Papers Meteor. Geophys.*, **2**, 234–262.

Mathur, M. B., 1972: Simulation of an asymmetric hurricane with a fine mesh multiple grid primitive equation model. Rept. No. 72-1, Dept. of Meteorology, Florida State University.

Matsuno, T., 1966: Numerical integrations of primitive equations by use of a simulated backward difference method. *J. Meteor. Soc. Japan*, **44**, 76–84.

Ooyama, K., 1966: On the stability of the baroclinic circular vortex: Sufficient criterion for instability. *J. Atmos. Sci.*, **23**, 43–53.

——, 1969: Numerical simulation of the life cycle of tropical cyclones. *J. Atmos. Sci.*, **26**, 3–40.

——, 1971: A theory of parameterization of cumulus convection. *J. Meteor. Soc. Japan*, **49**, 744–756.

Phillips, N. A., 1957: A coordinate system having some special advantages for numerical forecasting. *J. Meteor.*, **14**, 184–185.

Richtmyer, R. D., 1957: *Difference Methods for Initial Value Problems.* New York, Interscience, 238 pp.

Rosenthal, S. L., 1969: Preliminary results from numerical experiments with a primitive equation model designed to simulate the development of tropical cyclones. *Proc. WMO/IUGG Symposium on Numerical Weather Prediction*, III, Tokyo, 49–59.

——, 1971: The response of a tropical cyclone model to variations in boundary layer parameters, initial conditions, lateral boundary conditions, and domain size. *Mon. Wea. Rev.*, **99**, 767–777.

Sasamori, T., 1970: A numerical study of atmospheric and soil boundary layers. *J. Atmos. Sci.*, **27**, 1122–1137.

Senn, H. V., and H. W. Hiser, 1959: On the origin of hurricane rain bands. *J. Meteor.*, **16**, 419–426.

Simpson, R. H., 1954: Structure of an immature hurricane. *Bull. Amer. Meteor. Soc.*, **35**, 335–350.

Smagorinsky, J., 1963: General circulation experiments with the primitive equations: I. The basic experiment. *Mon. Wea. Rev.*, **91**, 99–164.

Staff Members, Tokyo University, 1969: Precipitation bands of typhoon Vera in 1959 (Part I). *J. Meteor. Soc. Japan*, **47**, 298–309.

Sundqvist, H., 1970: Numerical simulation of the development of tropical cyclones with a ten-level model. Part I. *Tellus*, **22**, 359–390.

Tatehira, R., 1961: A mesosynoptic and radar analysis of typhoon rain band, case study of typhoon "Helen," 1958. *Preprints Second Tech. Conf. Hurricanes*, Amer. Meteor. Soc., 115–126.

——, 1962: Analysis of rain band of Typhoon 5907 (in Japanese). *Kenkyu-Jiho*, **14**, 621–630.

Ushijima, T., 1958: Outer rain bands of typhoons. *J. Meteor. Soc. Japan*, **36**, 1–10.

Wexler, H., 1947: Structure of hurricanes as determined by radar. *Ann. N. Y. Acad. Sci.*, **48**, 821–844.

Yamasaki, M., 1968: Numerical simulation of tropical cyclone development with the use of primitive equations. *J. Meteor. Soc. Japan*, **46**, 178–201.

——, 1969: Large-scale disturbances in the conditionally unstable atmosphere in low latitudes. *Papers Meteor. Geophys.*, **20**, 289–336.

Yanai, M., 1961: Dynamical aspects of typhoon formation. *J. Meteor. Soc. Japan*, **39**, 282–309.

——, 1968: Evolution of a tropical disturbance in the Caribbean Sea region. *J. Meteor. Soc. Japan*, **46**, 86–109.